Manuscript accepted for publication in Journal of Structural Geology.

It has not yet been assigned a DOI or undergone the proofreading process.
Subsequent versions of the manuscript may have slightly different content.

Anamitra Sikdar
Dripta Dutta
Santanu Misra*

@anamitrasikdar
@driptadutta

Anamitra Sikdar
Dripta Dutta
Santanu Misra

Superplastic deformation inside the knife-sharp shear bands in mid-crustal granites

Anamitra Sikdar, Dripta Dutta, Santanu Misra*

Experimental Rock Deformation Laboratory, Department of Earth Sciences, Indian Institute of Technology Kanpur, Uttar Pradesh, 208 016, India

Abstract

We examined the microstructures of three ductile shear bands of granitic composition that deformed under mid-to-upper greenschist facies. These shear bands, from the Bundelkhand Craton, India, are 0.8-4.4 mm thick with 20-30 microns median grain sizes and share sharp contacts with the host granite. Comminution of the rheologically stronger feldspars increased permeability, promoted fluid influx, and allowed strain localisation in the incipient shear bands. The major components, quartz and feldspars, deformed via phase-specific crystal plastic deformation mechanisms. Quartz in the monomineralic bands deformed predominantly via dislocation creep, while the feldspars deformed via diffusion creep. Finer quartz grains, which occur at plagioclase triple junctions, resulted from myrmekitisation – also evident from the anti-clustered distribution of quartz-plagioclase phase boundaries and CPO inheritance. The weak CPOs and high mean misorientation angles of the fine plagioclase and K-feldspar grains and yet a high shear strain (γ = 16-37) suggest a significant contribution of grain boundary sliding (GBS) in strain localisation inside the ductile shear bands. Since intracrystalline slip alone cannot explain the high ductile strain in the shear bands, we suggest that GBS controlled the deformation and maturation of the shear bands and promoted superplasticity to accommodate further shearing.

Keywords:

Mylonitisation, EBSD, Grain boundary sliding, Phase mixing, CPO inheritance.

***Corresponding author:**

Santanu Misra (smisra@iitk.ac.in; +91 512 259 6812)

1. Introduction

Superplasticity enables materials to withstand tremendous strain, exceeding 400% tensile strain, while exhibiting minimal plastic deformation signatures, such as crystallographic preferred orientations (CPOs) (Chokshi et al., 1993; Langdon, 2009; Nguyen et al., 2020). Although primarily reported in metals as a product of grain boundary diffusion creep and sliding mechanisms (Edington et al., 1976; Sherby and Wadsworth, 1989; Chokshi et al., 1993), superplasticity also occurs in naturally deformed ultrafine-grained (<10 microns) rocks (Behrmann and Mainprice, 1987; Steffen et al., 2001; Kenkmann and Dresen, 2002). Fluid-driven metasomatic reactions and the consequent nucleation of phases lead to 'phase mixing', which inhibits grain growth by pinning and assists in maintaining a fine grain size in mylonites (Ishii et al., 2007; Czaplińska et al., 2015; Bercovici and Skemer, 2017; Ceccato et al., 2018; Alaoui et al., 2023). Mylonites often exhibit superplastic behaviour because grain size reduction and the presence of aqueous fluids, if any, both promote superplasticity (Schmid et al., 1977; Behrmann, 1985; Gilotti and Hull, 1990; Paterson, 1990).

Grain size reduction switches the deformation mechanism from the grain size insensitive (GSI) dislocation creep to grain size-sensitive (GSS) mechanisms, such as grain boundary diffusion (GBD) creep (Etheridge and Wilkie, 1979; Stünitz and Fitz Gerald, 1993; Kilian et al., 2011). GBD is further facilitated if the grain boundaries are 'wet' (Tullis et al., 1996). Grain boundary sliding (GBS), creep cavitation, and GBD creep are frequently identified as the active processes that lead to the maturity of 'wet' shear zones (Fusseis et al., 2009; Drury et al., 2011; Okudaira and Shigematsu, 2012). Under high ductile strain, polyminerallic mylonites consisting of equant-shaped grains with low dislocation densities can deform superplastically, with GBS

being one of the primary strain accommodating mechanisms (Boullier and Gueguen, 1975; White, 1977; Behrmann, 1985; Dimanov et al., 2007). GBS is either accommodated by stress-induced diffusion of vacancies (Lifshitz sliding) or by intragranular dislocation movement (Rachinger sliding) (Langdon, 2006). Both sliding mechanisms can operate simultaneously on different phases in naturally deforming rocks (Fliervoet et al., 1997; Lopez-Sanchez and Llana-Fúnez, 2018).

Mylonitisation in granitic rocks may occur along narrow, “knife-sharp” bands (Mandal et al., 2004; Mancktelow and Pennacchioni, 2005; Misra et al., 2009), which are characterised by elevated shear strain gradients than their vicinity. Such bands often develop along brittle precursors such as fractures, which enable strain localisation by allowing fluid-mediated reaction softening (Segall and Simpson, 1986; Imon et al., 2002; Mancktelow and Pennacchioni, 2005; Misra et al., 2009; Sarkar et al., 2020). In such cases, the absence of gradational shear band boundaries indicates confinement of the physical and chemical changes within the narrow space bounded by the shear band walls. Consequently, they are ideal candidates for identifying and assessing the deformation mechanisms that uniquely affected the shear band constituents. But such an assessment could be challenging due to the phase-specific flow law parameters (e.g., stress exponent, activation energy, etc.) at any given P-T condition (Tullis, 2002; Rybacki and Dresen, 2004; Lusk et al., 2021), and the spatial variations in deformation mechanisms due to the varying mineral abundances. For example, grains in a monophase quartz ribbons of mylonitic granites can deform via dislocation creep, whilst diffusion creep mechanism operates in the polyphase matrix (Ribeiro et al., 2019).

Therefore, the effects of spatial distribution of different phases on the mechanisms that cause and promote strain localisation within shear bands must be examined. To that end, we chose three narrow mylonitic and polymineralic ductile shear bands with 'knife-sharp' walls from the high-K anatectic granite of the Bundelkhand Granite and Gneissic Complex (BGGC). Our research delves into the intriguing phenomenon of grain boundary sliding (GBS) in the context of superplastic deformation, specifically focusing on crustal rocks like granitic gneiss that commonly contain prominent shear bands. Although GBS has been observed in the rock record before, its role in shear-band maturation and its unique superplastic behaviour has not been extensively explored in the existing literature. The studied shear bands have dissimilar phase distributions, allowing us to assess the phase-specific mechanisms leading to their superplastic deformation. The superplastic deformation in these crustal rocks with such specific grain sizes raises important questions about the underlying mechanisms and potential applications.

2. Geology

Bundelkhand Granite and Gneissic Complex (BGGC), one of the oldest cratonic blocks of the Indian Shield, covers ~26,000 square kilometres in central India (Kaur et al., 2016). High-K anatectic granite comprised nearly 40% of the BGGC. Tonalite trondhjemite granodiorite (TTG) gneisses and mafic rocks were the remaining components of the craton. However, subsequent upliftment and erosion of the TTGs and the supracrustal rocks exposed the granitoid batholith (**Fig. 1a**). At present, 90% of the areal exposure of the craton is high-K granitoid (Absar et al., 2009). The TTG gneisses record the oldest dates (3.55 Ga; Zircon, U-Pb) (Dey and Moyen, 2020). Episodic TTG magmatism throughout 250 – 850 Ma formed the basement of the craton. While

the TTG enrichment lasted till 2.7 Ga, the basement was further differentiated by partial melting products (e.g., sanukitoids, Closepet-type granitoid, anatectic K-rich granites and A-type granites) derived from crustal and mantle sources. This event lasted through 2.58 Ga till cratonic stability was attained in 2.50 Ga (Kaur et al., 2016; Singh and Slabunov, 2016; Joshi et al., 2017). The basement gneisses and schists experienced greenschist to amphibolite facies metamorphism (Basu, 1986), and a clockwise P-T path characterises the decompression of the craton (Pati, 2020).

Two distinct fluid fluxes in 2.2 Ga and 2.0 Ga (Rao et al., 2005; Pati et al., 2007) affected the craton and created two sets of conjugate linear fabric, which are filled by mafic dyke swarms and giant quartz veins (**Fig. 1a**). At least four deformation phases affected the BGGC from 3.3 – 2.5 Ga and produced four distinct sets of shear bands (Mondal et al., 2002). The E-W trending shearing event was the oldest (Singh and Bhattacharya, 2010). NW-SE and NE-SW are nearly coeval conjugate sets, and N-S trending deformation was the youngest among the events (Rao et al., 2005; Bhattacharya and Singh, 2013; Singh and Bhattacharya, 2017). The BGGC carries the imprints of 0.5-0.6 Ga old Pan-African event, responsible for the knife-sharp juvenile shear bands in the craton (Kaur et al., 2016; Sensarma et al., 2018). This event is preceded by the post ~2.5 Ga event of grey-granite to pink-granite transformation in the presence of fluids, which induced reactions in nominally anhydrous minerals like feldspars and increased the porosity of the granites (Putnis, 2021).

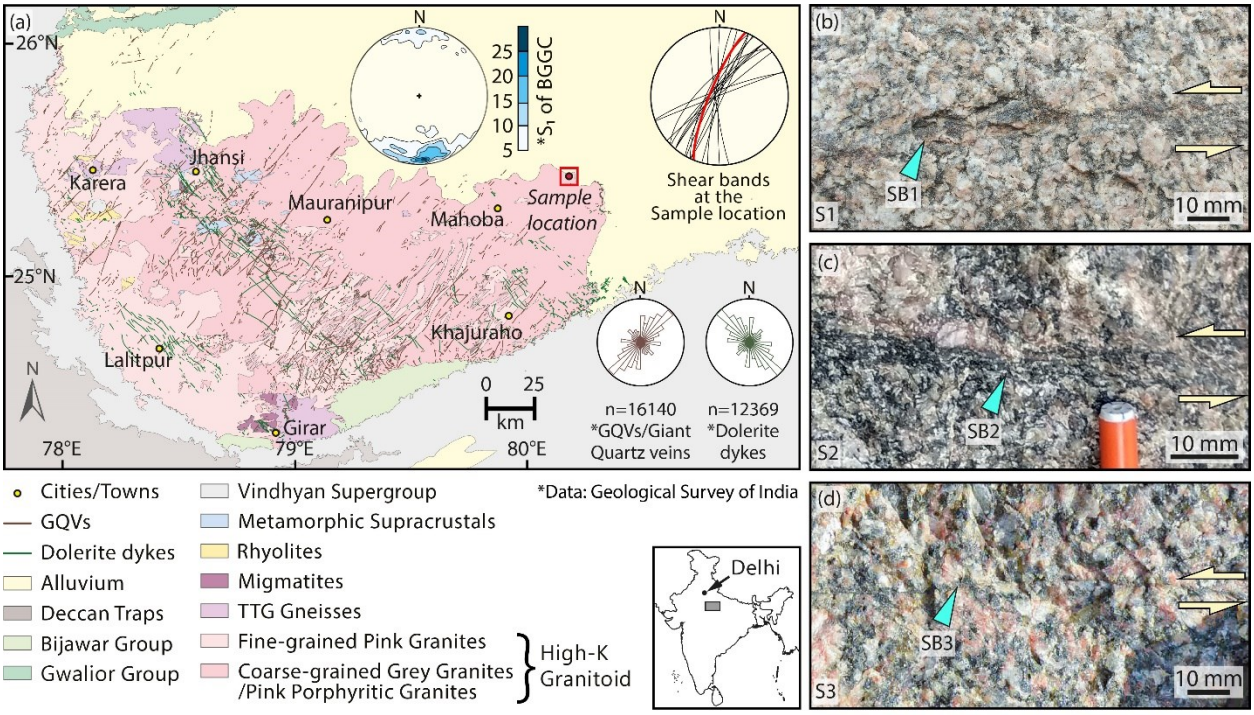

Fig. 1. *Study area and field observations. (a) Geological map of the Bundelkhand Craton with the major structural fabrics. The lower-hemisphere and equal-area projection at the top middle shows the orientation of the primary foliation (S_1 fabric) in the craton. Rose plots at the bottom right corner in the map represent the azimuthal distributions of the dolerite dykes and the giant quartz veins (GQVs also known as quartz reefs). The S_1 fabric data and the orientations of the dolerite dykes and GQVs are from the open data reserve of the Geological Survey of India (GSI). The lower-hemisphere and equal-area projection at the top right is the orientation of the shear bands at the sample location, marked by red square, and the red great circle is the mean orientation. Outcrop photographs of the high-K Anatectic granite samples (b) S1, (c) S2 and (d) S3 bearing the knife-sharp shear bands. Shear bands are marked by cyan arrowheads. Right side of the photographs (b) – (d) is SW.*

3. Methods

Three oriented samples (foliation: 202°/ 78° NW, lineation: sub-horizontal), S1, S2 and S3 (**Figs. 1b, c, d**), of medium-grained pink granite with visible ductile shear bands (SB1, SB2 and SB3, respectively) were collected from near Kabrai (25.44° N, 80.18° E) (**Fig. 1a**). The samples used in this study were located about 50 meters apart from each other and experienced approximately similar pressures and temperatures. The measured thicknesses of the shear

bands in the field are 3 mm (**Fig. 1b**: SB1), 4.5 mm (**Fig. 1c**: SB2) and 1 mm (**Fig. 1d**: SB3). The shear bands have sharp contacts with the host rock, i.e., they have a very high shear strain (γ: 16.2, 23.9, 37.3, respectively: **Supplementary Fig. SF1**). In the following discussions, we will be referring to them as 'knife-sharp' shear bands. Elongation of each band is calculated assuming the stretching of a line segment across the band in its initial condition. The values of stretch (*s*) are 1626%, 2394%, and 3732%, respectively (method described in the **Appendix**). The curved geometry of the displaced marker veins along the shear bands confirms that they are not fault-like shear bands or "sheared joints" as described by Pennacchioni and Mancktelow (2018). To understand the underlying mechanism for this superplastic behaviour, i.e., the unusually large strain in the shear bands, the samples are analysed under optical and EBSD-assisted scanning electron microscopes for detailed micro-texture analysis. A detailed account of the methods is described in the following paragraphs.

3.1. Optical and electron microscopy

The kinematic reference frame of the shear bands consists of the three mutually orthogonal X, Y, and Z axes of the finite strain ellipsoid (Ramsay, 1980), where X is the direction of the lineation, i.e., maximum stretching, and XY plane is approximated as the shear plane because of the very large strain. The samples hosting the shear bands SB1, SB2, and SB3 were sliced along their XZ sections i.e., parallel to the lineation and perpendicular to the shear plane. The thin sections were polished up to 0.25 microns (diamond paste) and observed using a transmitted light microscope.

We used broken surfaces of the three shear bands, mechanically fractured along the XZ planes, to observe the morphology of the grain boundaries and surfaces within the shear

bands. We picked the broken surfaces with tweezers and placed them over aluminium stubs using conductive silver paint. The top surfaces of the samples were then Au-coated to 20 nanometres and observed under a scanning electron microscope in secondary electron mode.

3.2. EBSD: sample preparation, data acquisition and processing

We acquired EBSD data from rock chips (1.2 × 2.5 sq. cm in area, 0.5 cm thick and polished with colloidal silica) of SB1, SB2, and SB3, representing the XZ planes of the kinematic strain ellipsoid. The EBSD data were collected using FEG SEM and AZtec data acquisition software. An accelerating voltage of 20 kV, 1.5 microns step size, and 12 mm acquisition distance were used along with a beam current of 10 nA and 70° sample tilt in low vacuum mode. The indexing rate ranged between 70-90%. Multiple scans were acquired with spatial overlaps of ~20% to cover the entire width of the shear bands.

We have used the MTEX toolbox v5.7.0 (Hielscher and Schaeben, 2008) in the MATLAB 2021a platform to post-process the raw EBSD data and stitch the EBSD maps. Poorly indexed points (mean angular deviation>1.5°) were discarded, and a threshold misorientation of 10° was used for grain reconstruction. Grains with less than five indexed pixels were also discarded. We also merged the twinned areas in quartz, plagioclase, and K-feldspar to their respective parent grains. We then assigned the mean orientation of the largest parent grain to the corresponding merged grains. The steps used to clean the EBSD datasets are outlined in **Supplementary Text S1**. Subsequent EBSD analyses were performed using the post-processed data for the major

phases (**Table 1**), i.e., quartz, plagioclase, and K-feldspar.

Table 1. *EBSD-derived relative area fractions (excluding non-indexed pixels) of the constituent minerals in each shear band.*

Sample Name	**Quartz (%)**	**Plagioclase (%)**	**K-feldspar (%)**	**Biotite (%)**	**Muscovite (%)**	**Chlorite (%)**
SB1	50.57	41.97	7.42	0.03	-	-
SB2	29.07	61.07	7.51	1.69	0.59	0.04
SB3	12.63	19.01	68.31	-	0.06	-

We used a one-point-per-grain approach to plot the pole figures, which are presented as equal-area and lower hemisphere projections. The CPO strengths are reported using texture (J, Bunge, 1982) and misorientation (M, Skemer et al., 2005) indices. We have also plotted the misorientation angle (MAD) and axis distributions (MXD). Core-to-rim misorientation line profiles are also presented for a few quartz grains exhibiting prominent subgrains outside and inside the shear bands (**Supplementary Text S2**). Area-weighted distributions of their long axes are plotted as rose diagrams to assess the shape-preferred orientation (SPO) of the grains within the shear bands. For the SPO analysis, we omitted grains with equivalent diameters below 4.5 mm (three times the step size of EBSD data acquisition) and those truncated by the EBSD map boundaries. We used the alignment factor (AF) of (Barraud, 2006) as a proxy for SPO strength (**Supplementary Text S3**).

We have also quantified the relative distribution (clustered, anti-clustered, random) of the quartz and plagioclase grains, using the grain (between the same phase) and phase (between different phases) contact frequencies inside SB1 and SB2 to identify possible spatial variations of deformation mechanisms. Areas dominated by quartz and plagioclase grains were particularly targeted. We selected three domains from SB2 based on the relative abundances of

quartz and plagioclase grains. Two of these three domains lie adjacent to and surround a K-feldspar porphyroclast and they are dominated by plagioclase. These two regions were targeted to gauge the extent of phase mixing. The porphyroclast is chosen from the core of SB2 to ensure that the contribution of the host rock grains on the studied phase spatial distribution was negligible. The third domain consists majorly monomineralic quartz bands. We omitted SB3 in this analysis as SB3 mostly consists of K-feldspar grains only. We coded (**Supplementary Text S4**) the algorithm outlined in Heilbronner and Barrett (2014) in MATLAB and used it in this study. A clustered distribution implies activity of plastic deformation of monophase aggregates, whereas an anti-clustered distribution suggests active phase mixing in the deforming polycrystalline aggregate (Heilbronner and Barrett, 2013). We performed similar phase distribution analyses in the thinner SB1 for the quartz and feldspar, but we could not observe porphyroclasts sitting at the core of SB1.

4. Results

4.1. Transmitted light microscopy

The average thicknesses of SB1 and SB2 are 3.3 and 4.4 mm, respectively, and SB3 is the thinnest (0.8 mm wide) (**Figs. 2a-f**). The margins of all the shear bands are sharp. The deflected gneissic foliation along the boundaries of SB1, SB2 and SB3 (**Figs. 2a-c)** and the sigmoidal polycrystalline quartz fishes within SB1 and SB2 (**Fig. 2a, b**) confirm the sinistral ductile shear sense, that is also observed in the outcrops (**Supplementary Fig. SF1**). Both SB1 and SB2 exhibit thread-like networks of fine biotite grains, which run parallel to the shear plane (**Figs. 2d, e**). These biotite grains (≈50 microns long) are significantly finer than those in the host rock (up to 200 microns long). In the higher magnification photomicrographs, the biotite grains appear

individually as either discontinuous fibres at low angles (5-30°) or parallel as a cluster to the shear plane (**Supplementary Fig. SF2**). The relict quartz grains constituting the ribbons in both B1 and SB2 consist of abundant subgrains (**Fig. 2g**) and grain boundary bulges (**Figs. 2h, i**).

Relict K-feldspar porphyroclasts within SB2 exhibit reaction fronts of albitisation progressing inside the porphyroclasts from their margins (**Figs. 3a-c**). Secondary quartz grains inside the myrmekitic plagioclase (more albitic than the parent) are identified by the difference in grey intensity and wormy appearance (**Figs. 3b-d**). Such myrmekitisation is also evident outside SB2 at the two feldspar phase boundaries (**Fig. 3d**). The feldspar grains in the host rock, along the shear band margins, are fractured (**Figs. 4a, b**). These fractures are connected to the shear bands and host quartz and feldspar fragments of sizes similar to the recrystallised quartzo-feldspathic grains that dominate the shear bands (**Figs. 4a, b**). The shear bands also contain sub-rounded feldspar porphyroclasts surrounded by recrystallised quartzo-feldspathic matrix (**Figs. 4c-f**). Some of these relict porphyroclasts have lobate nucleation sites along their boundaries and are mantled by finer recrystallised grains (**Supplementary Figs. SF3a, b**). These are the signatures of bulging (BLG) recrystallisation. A few feldspar grains in the host rock also exhibit flame-perthite texture (**Supplementary Fig. SF3c**).

The recrystallised feldspar grains within the shear bands are euhedral to subhedral (**Fig. 5a**). Close-up photomicrographs exhibit straight feldspar-feldspar grain boundaries within SB2 (**Fig. 5b**). Hourglass-shaped feldspar grains occupy the triple point phase intersections. (**Fig. 5c**). Quadruple intersections of feldspar grains are also observed within SB2 (**Fig. 5d**).

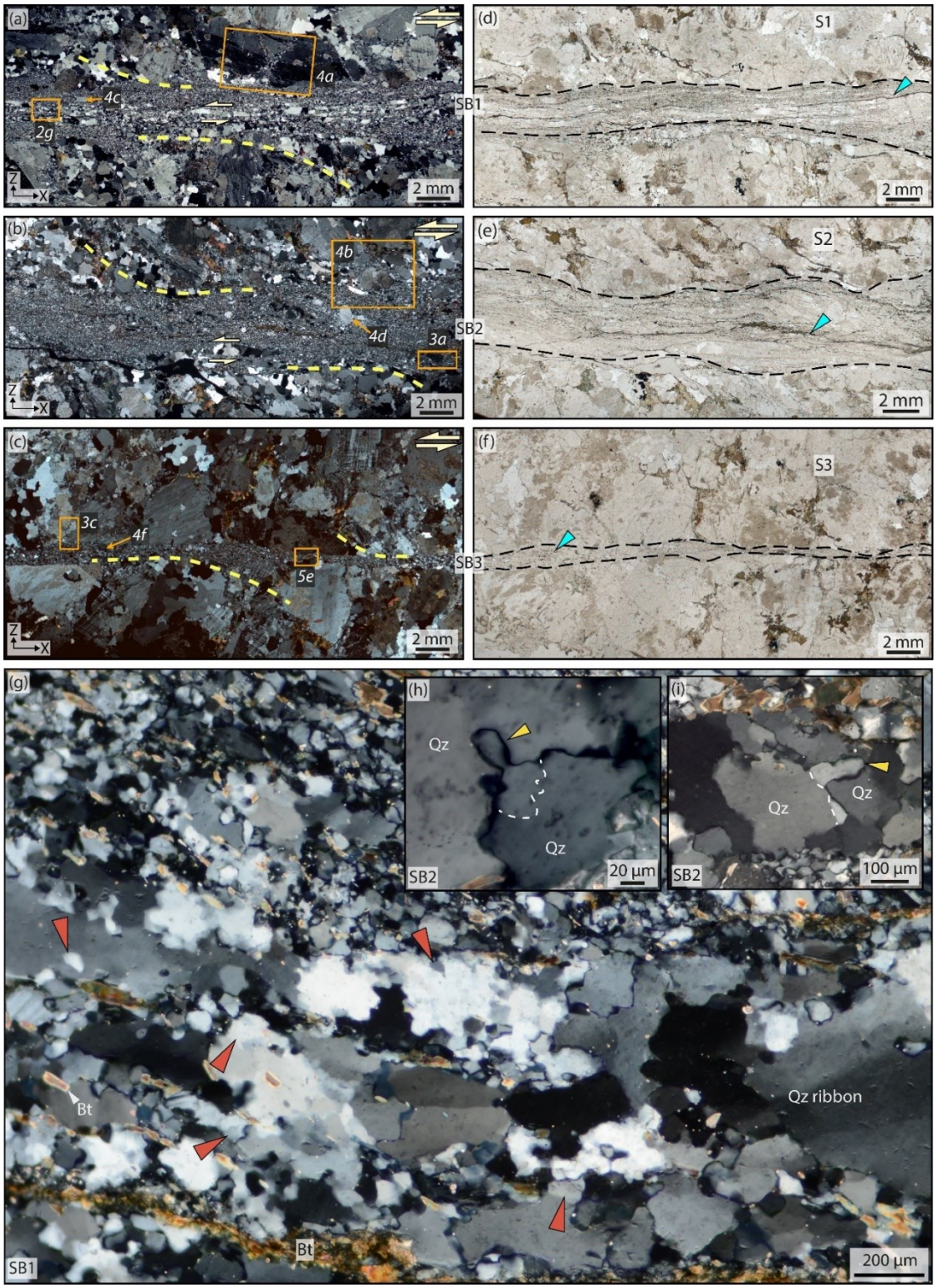

Fig. 2. *Photomicrographs of the shear bands. (a, d) SB1, (b, e) SB2 and (c, f) SB3. (a) – (c) are cross-polarised images. (d) – (f) are plane-polarised images. Black dashed curves demarcate the shear bands in (d) – (f). The deflected markers (yellow dashed curves) in (a) – (c) and sigmoid polycrystalline quartz aggregates in (a) and (b) indicate sinistral ductile shear senses. The*

orange boxes and arrows mark the locations of figures used in Figs. 2-5. The thread-like networks of phyllosilicate grains are shown using cyan arrowheads. Quartz deformation microstructures (g) – (i). Grain boundary migration bulges (yellow arrowheads) and subgrains (red arrowheads) in the quartz ribbons within SB1 and SB2. The bulges and subgrains are nearly the same sizes as the surrounding recrystallised quartz grains. The white dashed curves in (h) and (i) mark the visible subgrain boundaries near the bulges. The half-arrows in (a) – (c) indicate the overall shear senses. Right side of the photomicrographs (a) – (f) is SW. Mineral abbreviations are as per Whitney and Evans (2010).

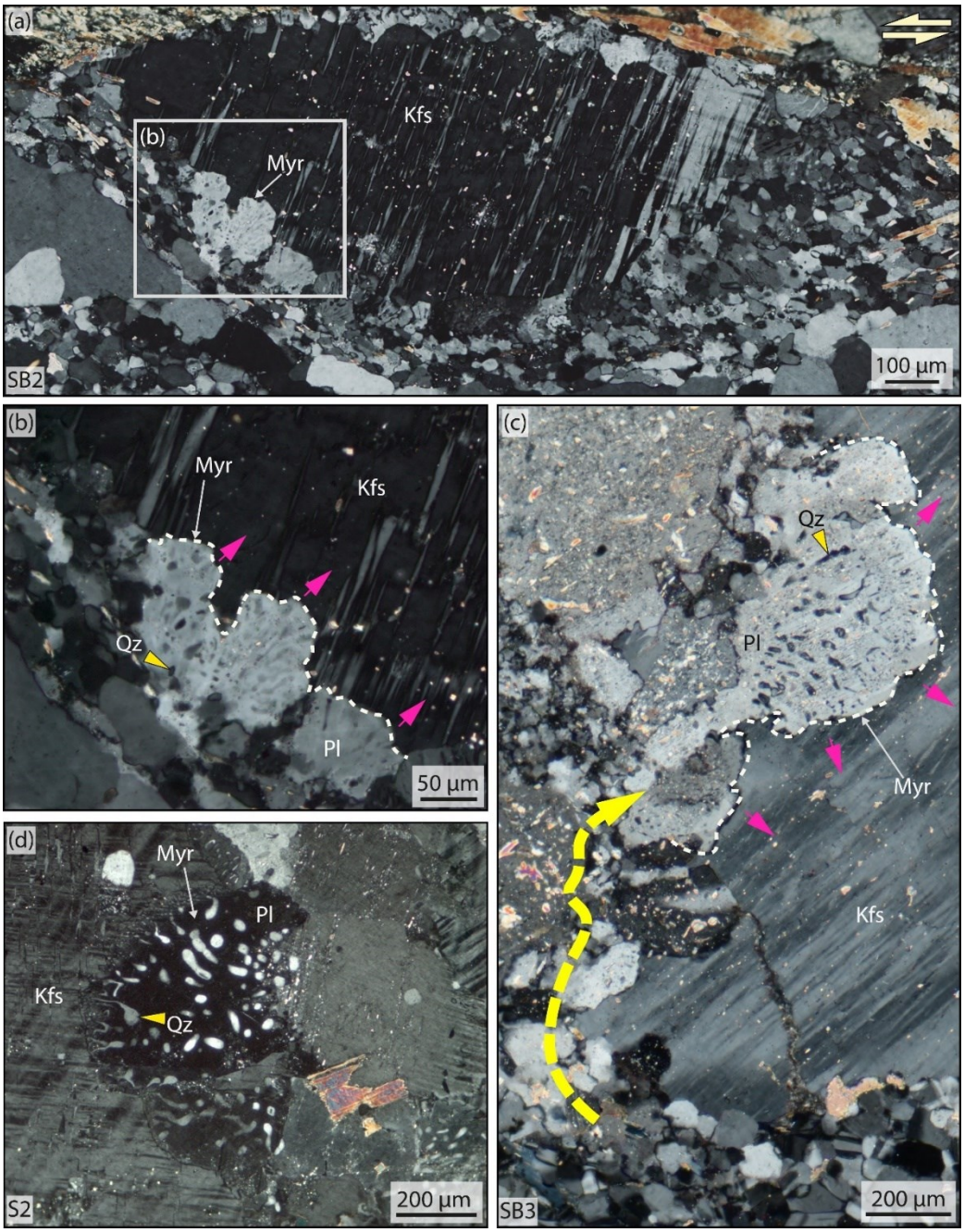

Fig. 3. *Myrmekitisation (Myr) in K-feldspar. (a) Deformation-induced myrmekitisation in the compressional zone of the relict feldspar porphyroclast within SB2. (b) – (c) Quartz neomineralisation inside the recrystallised feldspar grains (yellow arrowheads). White dashed curves in (b) and (c) demarcate the reaction front, and the pink arrows show the progression direction. Thick yellow dashed line with arrowhead refers to a possible fluid entry path from the incipient shear band. (d) Myrmekite at the two-feldspar phase boundary in the host rock S2. Tails of the wormy quartz inclusions (yellow arrowheads) in the myrmekite are connected to the reactant feldspar grain. Mineral abbreviations are as per Whitney and Evans (2010).*

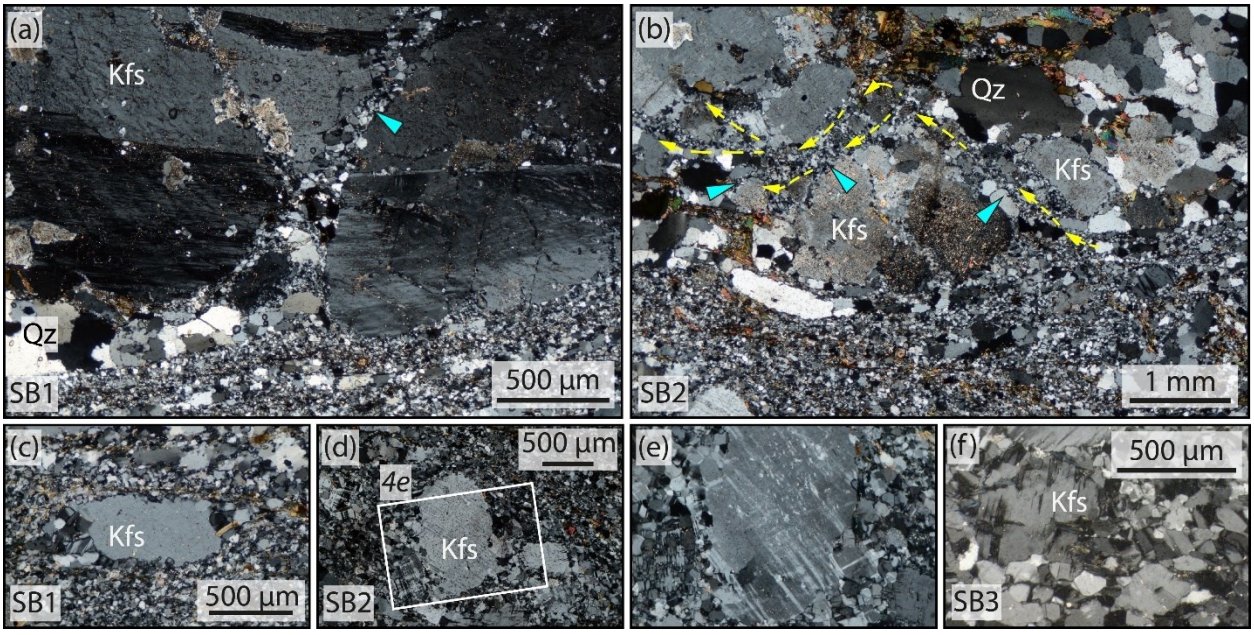

Fig. 4. *Brittle deformation of feldspar. (a) The fractured feldspar porphyroclast is adjacent to the upper margin of SB1. The fractures are filled with broken fragments of feldspar porphyroclasts (cyan arrowheads). (b) Anastomosing network (yellow dashed curves) of fine grain fragments along intragranular fractures (cyan arrowheads) connected to SB2. Isolated feldspar porphyroclasts within the fine recrystallised matrix of (c) SB1, (d, e) SB2, and (f) SB3. Mineral abbreviations are as per Whitney and Evans (2010).*

The core of SB2 consists of two types of phyllosilicates – (i) dusty anhedral grains of K-rich muscovite (sericite) (**Supplementary Fig. SF3d**), one of the myrmekitisation products of the feldspar grains, and (ii) anhedral biotite grains, which are parallel to the shear plane and occupy the spaces between the quartz and feldspar grains (**Fig. 5e**). Some of these biotite grains are observed to be replaced by chlorite grains, which warp around quartz and feldspar grains in SB3 (**Fig. 5f**). However, in SB3, biotite threads are observed to get deflected by a cluster of feldspar grains which share rough and uneven boundaries (**Supplementary Figs. SF3e, f**).

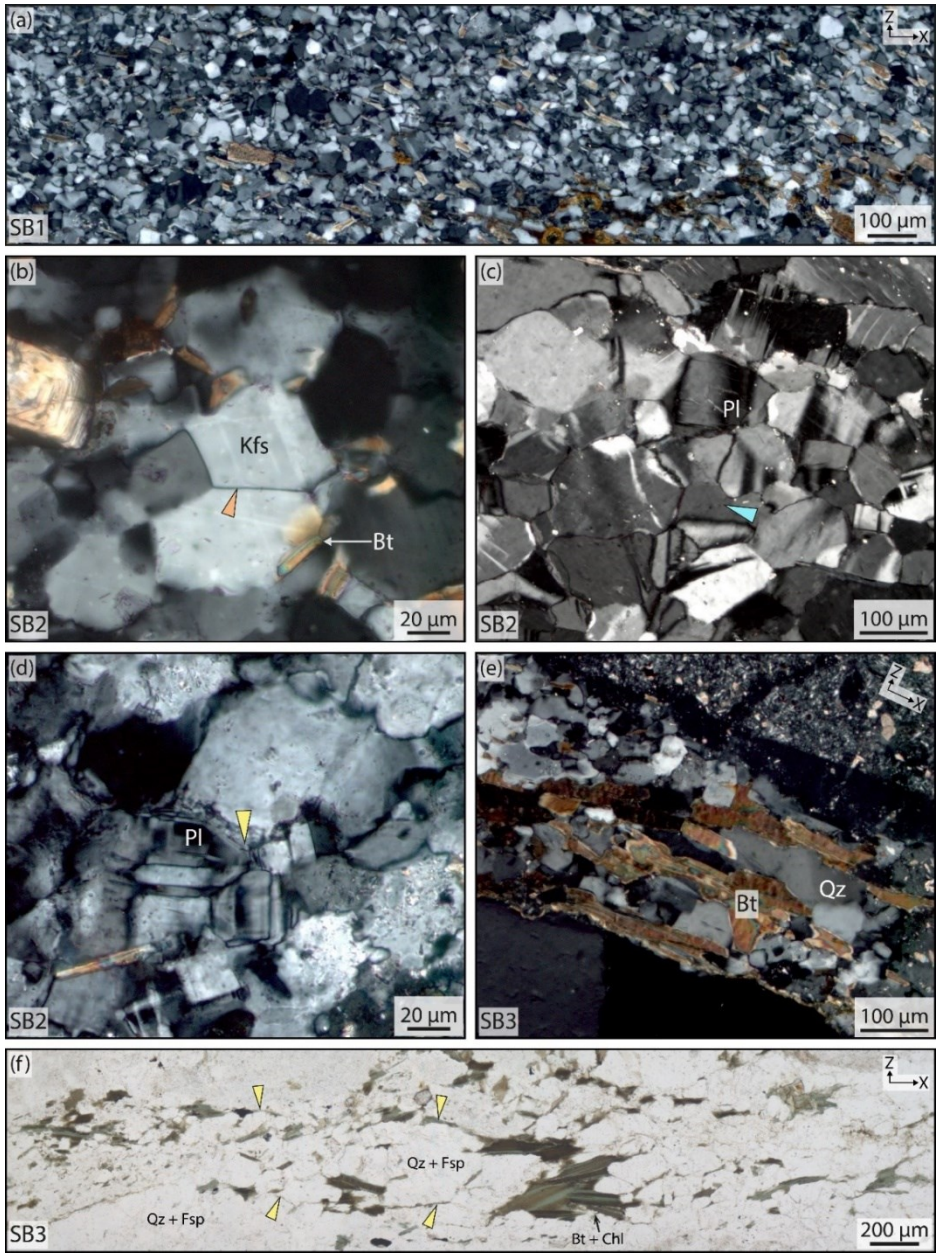

Fig. 5. *Grain boundary sliding microstructures and spatial arrangement of phyllosilicate grains. (a) Equant shapes of the fine recrystallised grains within the quartzo-feldspathic domain in SB1. (b) Straight feldspar grain boundary (orange arrowhead). (c) Feldspar crystallisation within hourglass-shaped intergranular space (cyan arrowhead). (d) Quadruple junction of feldspar grains (yellow arrowhead). Both (c) and (d) suggest past activity of neighbour pair switching mechanism. (b) – (d) suggest the sliding process was achieved by Lifshitz GBS. (e) A preferred arrangement of the elongated biotite grains within the intergranular spaces of SB3. (f) Thread-like network of the phyllosilicate grains warping around (yellow arrowheads) the quartz and feldspar grains. Mineral abbreviations are as per Whitney and Evans (2010).*

4.2. Broken surface SEM

The pores on the quartz grain surfaces are pyramidal, and adjacent pores are coalesced into cavities (**Fig. 6a**), which appear like low-angle grain surfaces. Wherever there is a high-density distribution of the pores on the grain surface, the coalescence of pores results in channel formation (**Fig. 6a**: white arrowhead). Linear valleys, ridges, and bulges are found on the feldspar grain surfaces (**Figs. 6b, c**). The surfaces also preserve voids left by grains of the counterpart split half (**Fig. 6b**). The articulations on the feldspar grain surfaces are nodule-like, and they appear to be part of the mother feldspar grains. The interstitial spaces of feldspar are not clean like the quartz triple junctions. Quartz and feldspar phases are observed at the junctions. The quartz grain surfaces are relatively smoother, and grain junctions are straighter (**Fig. 6a**) than those of the feldspars (**Figs. 6b, c**).

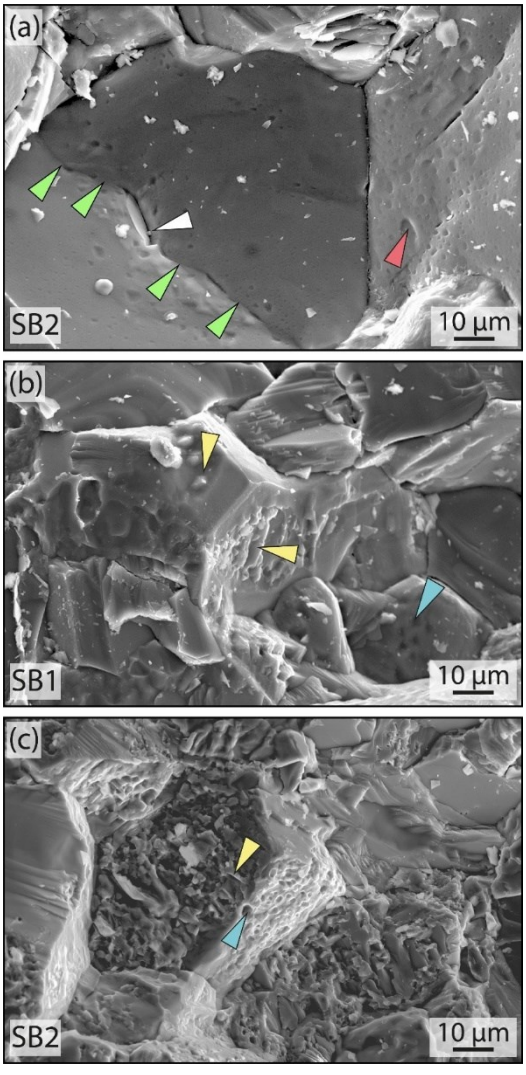

Fig. 6. *Split surface SEM images (a) – (c). (a) Quartz grain surfaces bearing isolated (red arrowheads) and coalesced (white arrowhead) pores. A possible subgrain wall is marked by green arrowheads. (b, c) Positive (yellow arrowheads) and negative (cyan arrowheads) structures on feldspar grain surfaces. See Sec. 4.2 for a detailed description.*

4.3. EBSD analysis

The EBSD-derived phase maps illustrate that the core of SB1 is dominated by monomineralic ribbons of quartz (**Figs. 7a)**. In contrast, the quartz ribbons in SB2 are present near the margins **(Fig. 7b**). SB3, on the other hand, is composed mainly of K-feldspar and plagioclase grains with very few quartz grains (**Fig. 7c**). The relative area fractions of the phases are provided in **Table 1**. The plagioclase-rich domains in SB1 and SB2 contain isolated quartz grains (**Figs. 7a, b**). Isolated K-feldspar grains occur throughout SB1, whereas in SB2, they occupy the margins (**Fig. 7b**) and the vicinity of the K-feldspar porphyroclast at the centre. The EBSD data for the quartz-rich and plagioclase-rich domains for both SB1 and SB2 are separately analysed. Because SB3 lacks such spatial mineralogical variation, the data for the entire band are analysed together.

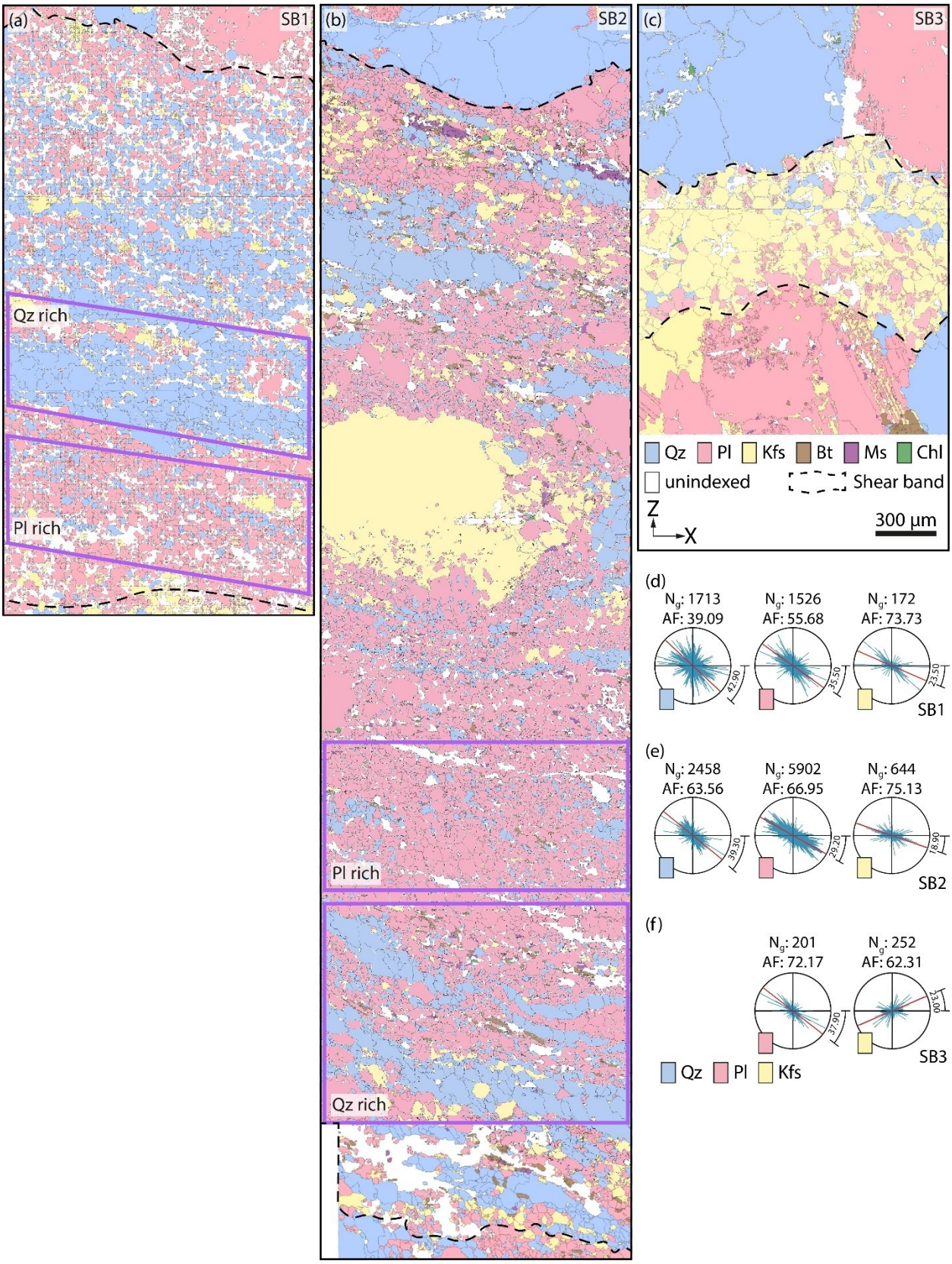

Fig. 7. *EBSD-derived phase maps of (a) SB1, (b) SB2 and (c) SB3. Purple solid boxes are quartz*

and plagioclase-rich regions used for EBSD analyses. (a) and (b) have same scale, legend, and orientation as those of (c). The black dashed curves demarcate the shear bands. Mineral abbreviations are as per Whitney and Evans (2010). (d) – (f) Rose plots illustrating the shape preferred orientations of the long axes of quartz, plagioclase, and K-feldspar grains. The column for quartz in SB3 is blank in (f), owing to fewer quartz grains in SB3. The red lines mark the average direction of the long axes for each plot. The values to the right of each plot show the angle between the average orientation and the shear plane. N_g: number of grains. AF: alignment factor. AF quantifies the strength of each plot (Barraud, 2006).

4.3.1. Shape Preferred Orientation

The three phases exhibit prominent shape-preferred orientations (SPOs) in SB1 (**Fig. 7d** and SB2 (**Fig. 7e**). Their SPOs in SB2 are relatively stronger than in SB1, as indicated by the corresponding alignment factors (AFs). The AFs of quartz, plagioclase, and K-feldspar in SB1 are 39.09, 55.68, and 73.73, respectively. In SB2, the AFs are 63.56, 66.95, and 75.13 (in the same order). In both SB1 and SB2, the long axes of the mineral grains show preferential alignment synthetic to the overall shear senses inferred from the outcrop (**Supplementary Figs. SF1**) and confirmed from the deflected markers adjacent to and the sigmoidal polycrystalline quartz fishes within SB1 (**Fig. 2a**) and SB2 (**Fig.2b**). However, in SB3, the long axes of plagioclase and K-feldspar grains are oppositely oriented (**Fig. 7f**). The SPO of the quartz grains in SB3 is not shown due to the fewer than 50 grains. The AFs of plagioclase and K-feldspar in SB3 are 72.17 and 62.31, respectively. The mean of the long axis orientations of quartz, plagioclase, and K-feldspar grains are approximately at ~40°, ~30-37°, and ~20-23°, respectively, to the shear planes indicated by the horizontal lines in the rose plots.

4.3.2. Crystallographic Preferred Orientation

Quartz (0001) CPOs in the quartz-rich domains of SB1 and SB2 show point distributions parallel to and at a low-angle, respectively, to the XY-plane. The maxima for SB1 lies on the

shear plane, whereas for SB2, it is oblique to the shear plane. The J and M indices of SB1 (J: 1.56, M: 0.04) and SB2 (J: 1.81, M: 0.06) suggest that the overall CPOs are weak. Both *m*{10-10} and *a*{11-20} CPOs of SB1 and SB2 exhibit non-random distributions, with the girdles being nearly parallel to their respective XZ-planes (**Figs. 8a, c**). In plagioclase-rich layers, the quartz CPOs are nearly random. The J and M indices of the CPOs in SB1 (J: 1.46, M: 0.01) and SB2 (J: 1.59, M: 0.02) suggest that they are weaker than those of the quartz-rich layers (**Figs. 8b, d**). In SB3, there are 55 quartz grains only, and the CPO distributions are random (**Fig. 8e**).

The plagioclase CPO distributions are more varied than those of quartz. Overall, they are random but relatively stronger in SB1 (J: 2.79, M: 0.02 for quartz-rich and J: 2.18, M: 0.02 for plagioclase-rich) than in SB2 (J: 1.74, M: 0.01 for quartz-rich and J: 1.62, M: 0.01 for plagioclase-rich) (**Figs. 8a-d)**. (100) maxima are nearly orthogonal to the foliation pole in both the shear bands (**Figs. 8a-d)**. The CPOs in SB3 are random but the J (6.46) and M (0.05) indices are higher than those in the other two shear bands (**Fig. 8e**).

K-feldspar CPOs, on the other hand, have fewer data points than the other two phases in both SB1 (81 and 31 in quartz-rich and plagioclase-rich domains, respectively) and SB2 (74 and 19 in quartz-rich and plagioclase-rich domains, respectively) (**Figs. 8a-d**). In SB3, they exhibit isolated point distributions, with the maxima being oblique to all the three kinematic axes of the strain ellipsoid (**Fig. 8e**). The J and M indices for K-feldspar CPOs in SB3 are 2.7 and 0.02, respectively.

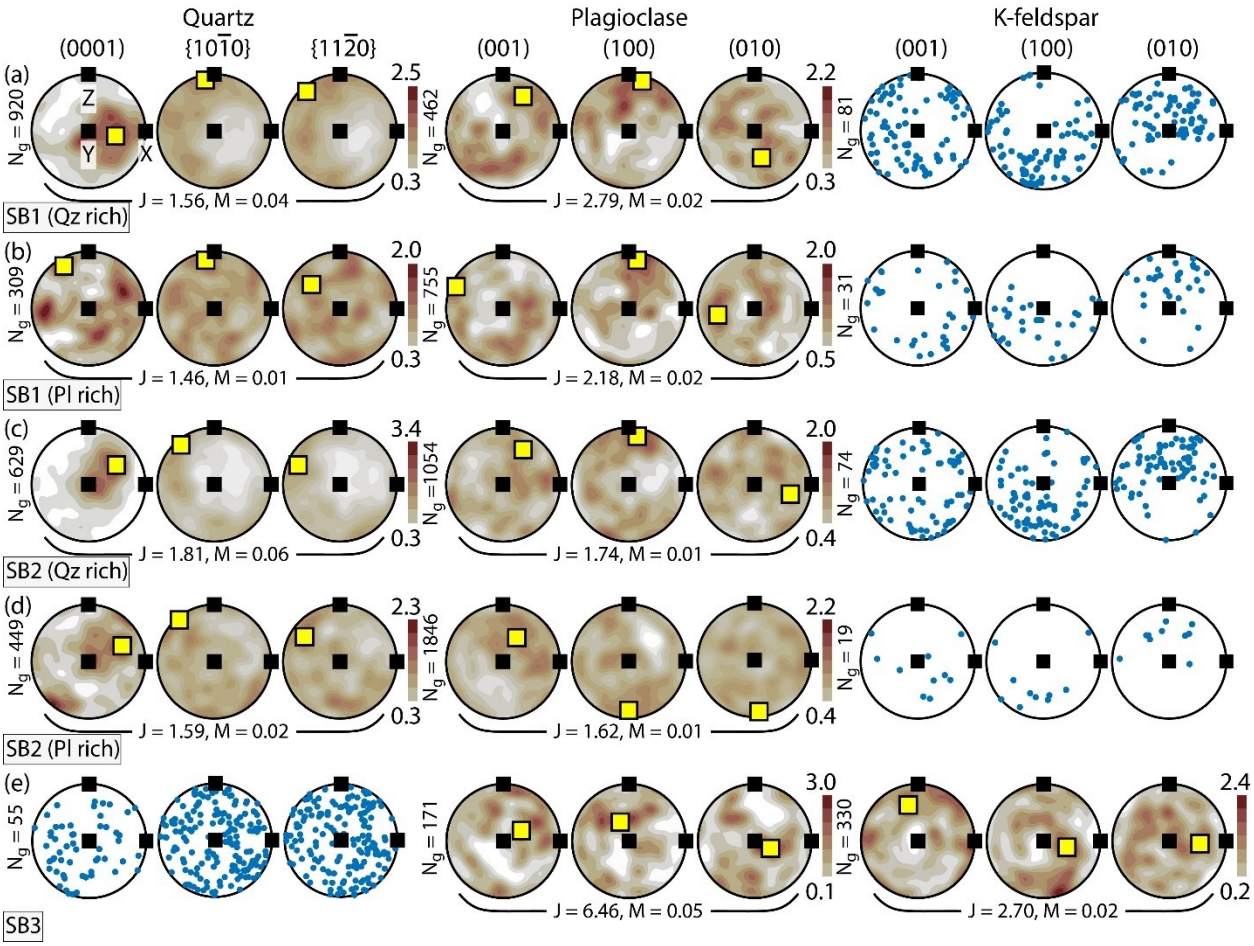

Fig. 8. *Quartz, plagioclase, and K-feldspar crystallographic preferred orientation plots (one-point-per-grain). (a, b) SB1, (c, d) SB2 and (e) SB3. These equal-area and lower hemisphere projections are contoured to multiples of uniform density (MUD); the minimum and maximum values are at the bottom and top of the vertical bars, respectively. Contouring is avoided when there are fewer than 100 grains. The yellow boxes denote points of maximum intensity. The 'bilbao' colour map of Crameri (2018) is used here. N_g: number of grains, J: J-Index (Bunge, 1982), and M: M-Index (Skemer et al., 2005). Mineral abbreviations are as per Whitney and Evans (2010).*

4.3.3. Misorientation analyses

The uncorrelated misorientation angle distributions (MADs) of quartz in the quartz-rich domains of SB1 (**Fig. 9a**) and SB2 (**Fig. 9c**), and in SB3 (**Fig. 9e**) are slightly different from the theoretical distributions. However, the uncorrelated and the theoretical MADs of quartz in the plagioclase-rich domains in SB1 (**Fig. 9b**) and SB2 (**Fig. 9d**) are nearly similar. The correlated

MADs of quartz, on the other hand, are different from both the uncorrelated and theoretical distributions in all the shear bands (**Fig. 9**). The uncorrelated MADs of plagioclase in both the domains in SB1 (**Figs. 9a, b**) and SB2 (**Figs. 9c, d**), and in SB3 (**Fig. 9e**) mimic the corresponding theoretical distributions. The misfit between the correlated MADs with the corresponding uncorrelated and theoretical distributions of plagioclase, is much less in SB1 (**Figs. 9a, b**) and SB2 (**Figs. 9c, d**), but higher in SB3 (**Fig. 9e**). The uncorrelated MADs of K-feldspar deviate from the theoretical distributions for all the domains in SB1 (**Figs. 9a, b**) and SB2 (**Figs. 9c, d**), but mimics it in SB3 (**Fig. 9e**). The correlated MADs differ from both the uncorrelated and theoretical distributions in all the shear bands. Although each phase shows high frequencies of correlated misorientations at low-angles (2-10°), the frequencies of uncorrelated MADs are higher than the correlated ones at angles >30° for quartz and >50° for the feldspars. The frequencies of correlated MADs are significantly lower than the uncorrelated at higher angles for each phase in SB3 (**Fig. 9e**). The mean of correlated misorientation angles, excluding those <10°, vary between 50-57° for the quartz grains in all the shear bands. The same occurs at 123-127° and 74-103° for plagioclase and K-feldspar, respectively, except for the K-feldspar in the plagioclase-rich domain of SB2 (171.44°). The average, including the low-angle misorientations (blue dashed lines in **Fig. 9**), is 27-34° for quartz in SB1 and SB2 and ~15° in SB3. These averages are 84-93° for the plagioclase grains in SB1 and SB2 and 31.88° in SB3. K-feldspar grains exhibit averages between 22-41° across all three shear bands except for the plagioclase-rich domain of SB2 (9.96°).

The low-angle (2-10°) misorientation axes of the three phases show strong non-random distributions in the crystal reference frames. For the quartz grains, they are mostly parallel to

the c-axis in all the shear bands (**Fig. 9**) except for the plagioclase-rich domain of SB1 in which most of them plot in between *r*{-1101} and *m*{10-10}. Some of the axes in the plagioclase-rich domains of SB1 (**Fig. 9b**) and SB2 (**Fig. 9d**), and in SB3 (**Fig. 9e**) are also near-parallel to the pole to *a*{11-20}. In the case of plagioclase grains, the distributions form girdles nearly parallel to (010) with maxima being parallel to both [-100] (SB1 and SB3) (**Figs. 9a, b, e**) and [001] (SB2) (**Figs. 9c, d**). The K-feldspar misorientation axes are mostly parallel to [001], but some of them in SB2 (**Figs. 9c, d**) and SB3 (**Fig. 9e**) are parallel to [010].

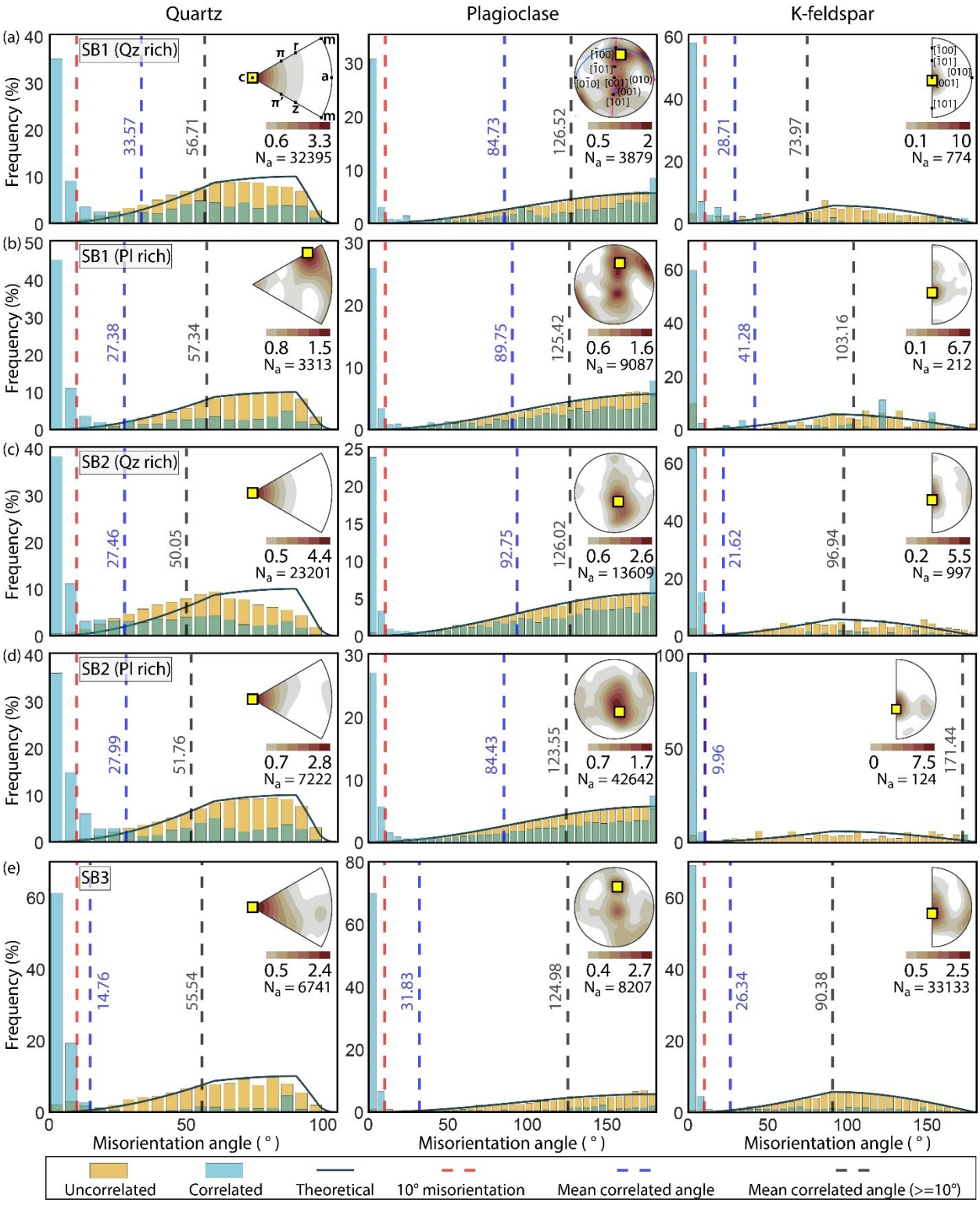

Fig. 9. *Misorientation angle and low-angle (2-10°) misorientation axis distributions. (a, b) SB1, (c, d) SB2 and (e) SB3. The red dashed lines mark the 10° misorientation. The blue and black dashed lines indicate the mean misorientation angles of the correlated distributions considering*

≥2° and ≥10° misorientations, respectively. The low-angle (2-10°) misorientation axis distributions on crystal coordinate systems are added as insets in the respective subplots. Each plot is contoured to multiples of uniform density (MUD); the minimum and maximum values are at the bottom left and right of the horizontal bars. The yellow boxes denote points of maximum intensity. N_a: number of axes. The 'bilbao' colour map of Crameri (2018) is used here. Some important crystallographic axes are marked for each phase in the top panel.

The distribution of misorientation axes corresponding to the higher angles (>10°) are more varied across the samples among the feldspars than quartz (**Fig. 10**). The axes corresponding to the 10-60° misorientations are all parallel to the pole to c(0001) of quartz except for a few in SB3 which are nearly parallel to the pole to *m*{10-10}. The quartz misorientation axes for 60-110° interval are at low angles to *r*{-1101} (**Fig. 10**). The high-angle misorientation axes distributions are relatively more random in the case of both plagioclase and K-feldspar (**Fig. 10**). The plagioclase misorientation axes in SB3 occur as isolated point distributions, whereas, in the case of K-feldspar, all the misorientation axes corresponding to the angular range 40-160°, occur at high angles to [010] (**Fig. 10**).

Maps depicting the intragranular misorientation at each pixel with respect to the mean orientation of the grain, henceforth referred to as MTEX mis2mean, and misorientation line profiles of selected quartz grains adjacent to, but outside, the top margin of SB2 (**Fig. 11a, Supplementary Figs. SF4a, b, c**) and SB3 (**Fig. 11b, Supplementary Figs. SF4d, e, f**), are also shown. The mis2mean maxima for these grains range from 8-17°. The cumulative misorientation (point-to-origin) exhibits a gradual increase from the cores to the rims of the grains, and the corresponding maxima lie within 3-12°. The mis2mean maxima for quartz grains that form the ribbons in SB1 (**Fig. 11c, Supplementary Figs. SF5a, b, c**) and SB2 (**Fig. 11d, Supplementary Figs. SF5 d, e, f**) ranges from 8-25°, and the maxima of cumulative

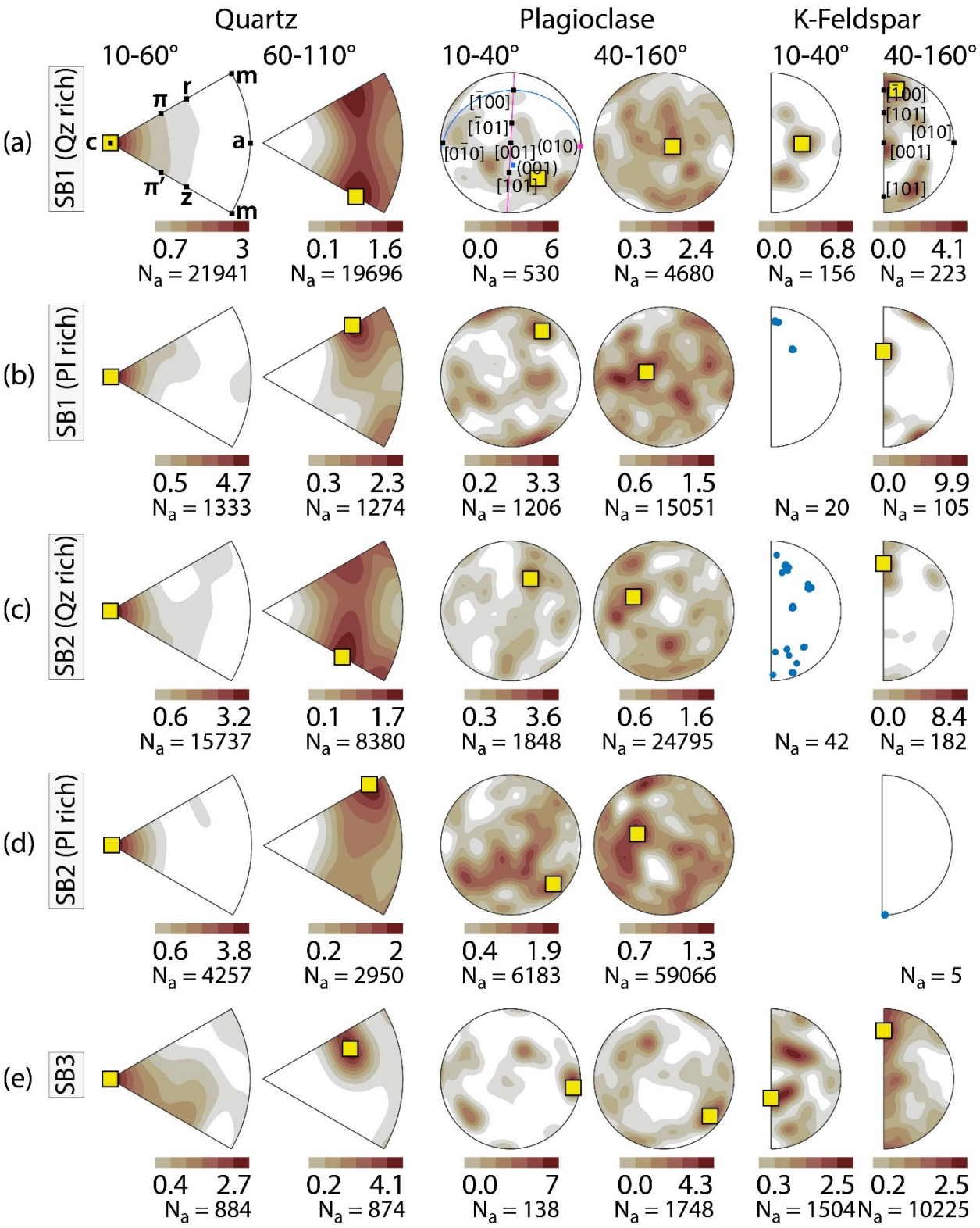

Fig. 10. *High-angle (≥10°) misorientation axis distributions on crystal coordinate systems. (a, b) SB1, (c, d) SB2 and (e) SB3. Each plot is contoured to multiples of uniform density (MUD); the*

minimum and maximum values are at the bottom left and right of the horizontal bars. The yellow boxes denote points of maximum intensity. N_a: number of axes. The 'bilbao' colour map of Crameri (2018) is used here. Contouring in some subplots is avoided because there are fewer than 100 axes. Some important crystallographic axes are marked for each phase in the top panel.

misorientation along the line profiles varies within 7-18°. The point-to-point misorientation profiles for quartz grains outside the shear bands exhibit fewer sharp peaks than those within the bands. The presence of subgrains in all these grains is prominent from the mis2mean maps. A few more mis2mean maps and misorientation line profiles are included in the **Supplementary Figs. SF4, SF5**.

4.3.4. Phase mixing and distribution

The spatial variabilities in the distribution of the phases within SB1 and SB2 are prominent. The top and bottom layers of a K-feldspar porphyroclast at the SB2 core (**Fig. 7b**) are analysed. In one such domain (**Fig. 12a**), where the c-axes of the quartz and plagioclase grains exhibit nearly random distributions (**Fig. 12b**), Q-Q (quartz-quartz) grain boundaries (**Fig. 12c**) are less abundant than P-P (plagioclase-plagioclase) grain boundaries (**Fig. 12d**) and Q-P (quartz-plagioclase) phase boundaries (**Fig. 12e**). In the second domain (**Fig. 12f**), the c-axes of the phases are less random (**Fig. 12g**) but the abundance of grain (**Figs. 12h, i**) and phase boundaries (**Figs. 12h, i, j**) is similar to that of the previous one (**Figs. 12c-e**). The contact probability versus quartz surface fraction plot for both these regions indicates higher randomness in the distribution of the Q-Q grain boundaries compared to the ordered distribution of both P-P grain boundaries and Q-P phase boundaries (**Fig. 12k**). Isolated quartz grains occupying the interstitial spaces of the feldspar grains is evident from the EBSD-derived

phase maps (**Figs. 12a, f**) as well as the thin-section (**Fig. 12l**). In the third domain (**Fig. 12m**), the quartz: plagioclase area fraction is ~1. The c-axes of quartz grains are preferentially oriented, unlike those of the plagioclase grains (**Fig. 12n**). In contrast to the rest, the Q-Q (**Fig. 12o**) and P-P grain boundaries (**Fig. 12p**), as well as Q-P phase boundaries (Fig. 11q), are almost equally numerous and exhibit clustered distributions (**Fig. 12k**). Similar results are obtained analysing chosen regions of SB1 (**Supplementary Fig. SF6**).

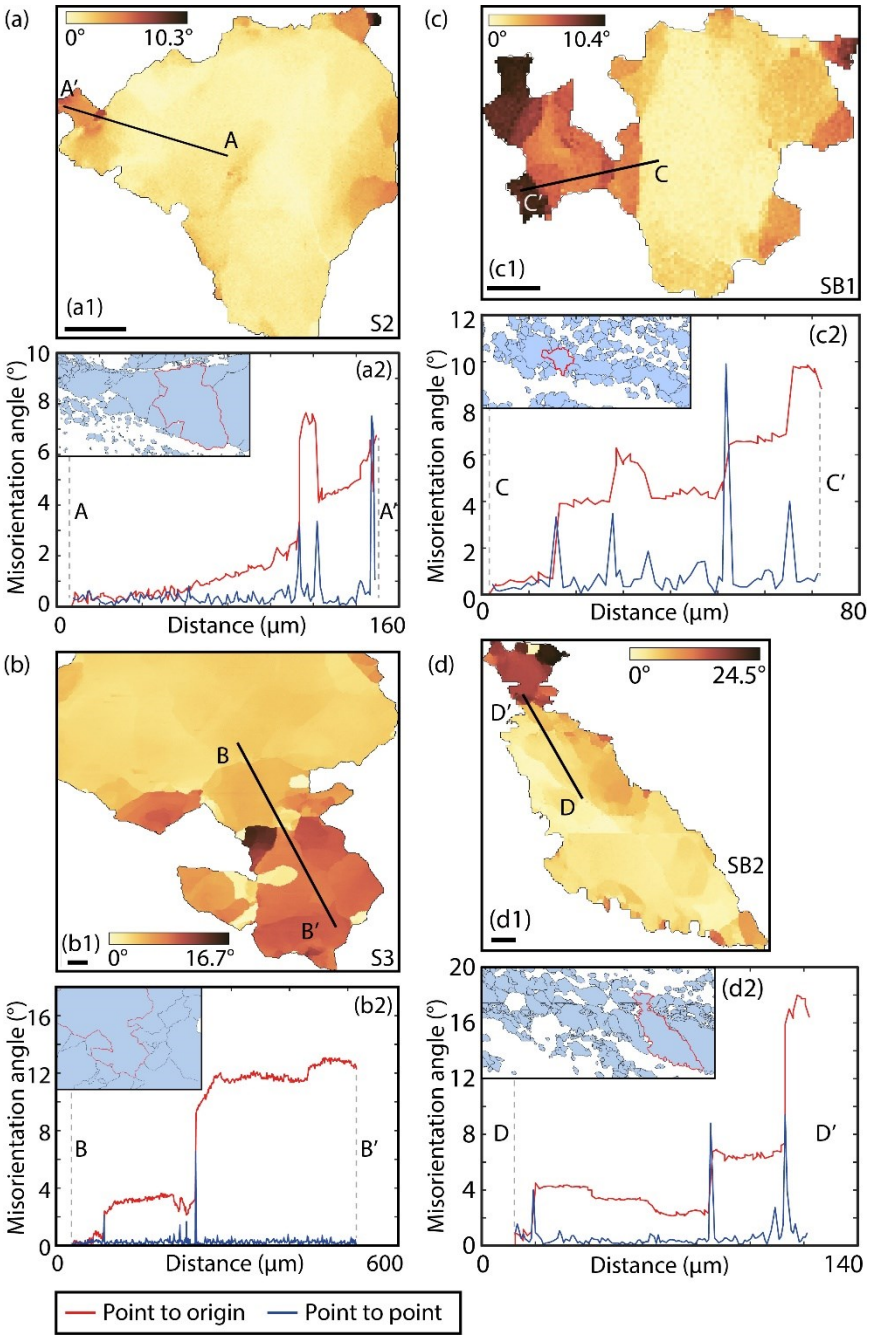

Fig. 11. *Misorientation to mean orientation (mis2mean) maps of selected quartz grains of the host rock (outside the shear bands) and the core-to-rim misorientation line profiles. (a) S2 (outside SB2). (b) S3 (outside SB3). (c) SB1. (d) SB2. The misorientation profile for each grain is shown right below it. Both 'point-to-origin' (red) and 'point-to-point' (blue) misorientation profiles are shown. The grains of interest are shown in the inset phase maps. The complete phase map of (a, d) is in* ***Fig. 7b****, of (b) is in* ***Supplementary Fig. SF10,*** *and that of (c) can be seen in* ***Fig. 7a****. All the black bars present below the mis2mean maps are 50 mm long for (a, b) and 25 mm long for (c, d). The 'lajolla' colour map of Crameri (2018) is used here.*

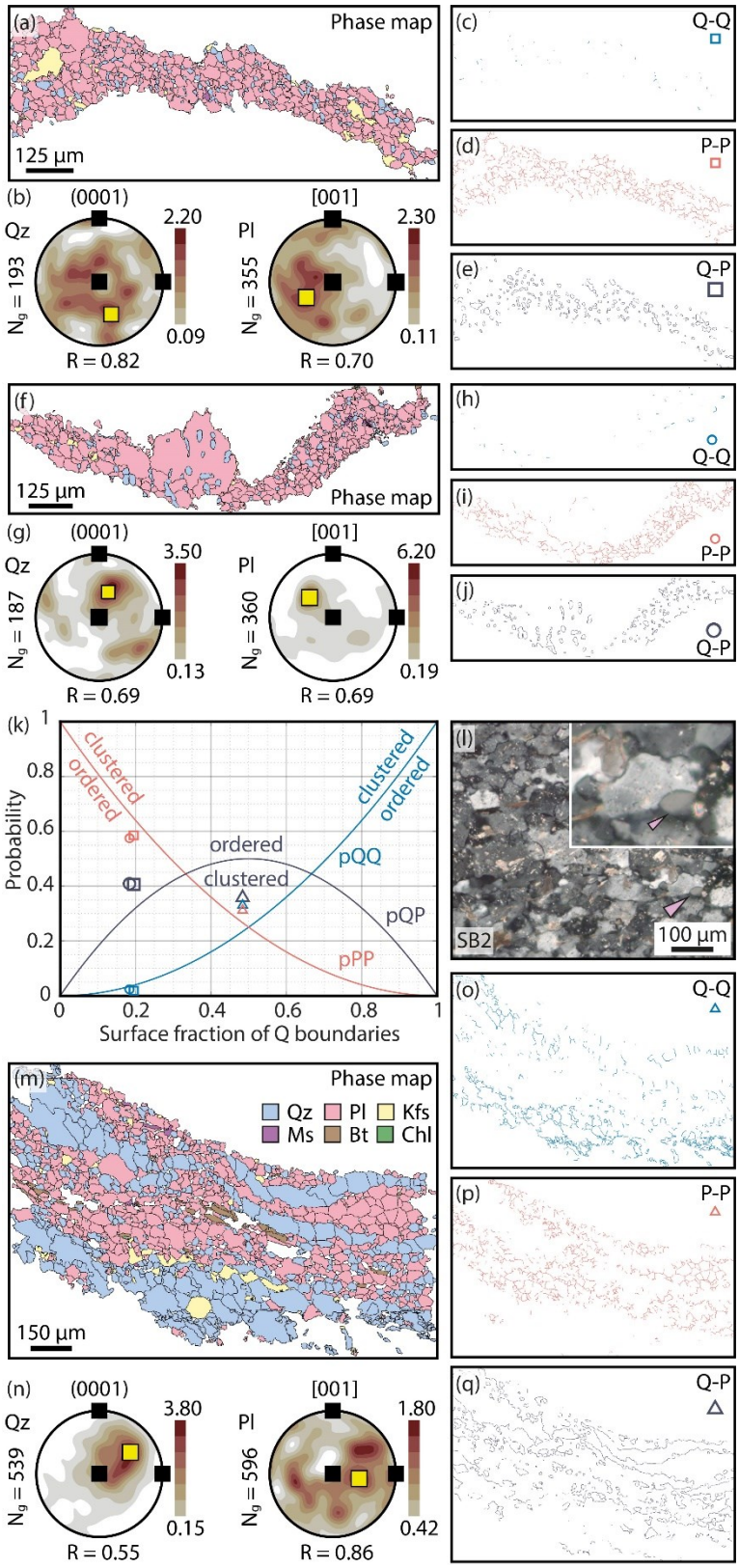

Fig. 12. *Phase spatial distribution analyses in SB2. (a) Phase map of a myrmekite domain from the upper margin of the K-feldspar porphyroclast within the shear band. (b) equal-area projections of c-axis CPOs of the quartz and plagioclase grains (one-point-per-grain). (c) Quartz grain boundaries. (d) Plagioclase grain boundaries. (e) Quartz-Plagioclase phase boundaries. (f) Phase map of a myrmekite domain from the lower margin of the same K-feldspar porphyroclast. (g) c-axis equal-area projections of the quartz and plagioclase grains (one-point-per-grain). (h) Quartz grain boundaries. (i) Plagioclase grain boundaries. (j) Quartz-Plagioclase phase boundaries. (k) Grain contact probability v/s surface fraction of quartz boundaries plot. The theoretical probabilities expected for randomly distributed quartz (pQQ) and plagioclase (pPP) grain boundaries and quartz-plagioclase (pQP) phase boundaries are illustrated by the continuous curves. (l) Cross-polarised photomicrograph showing the distribution of quartz grains at feldspar triple junctions like those visible in the EBSD-derived phase maps (a) and (b). (m) Phase map of a domain with quartz ribbons from near the bottom margin of the shear band. (n) c-axis equal-area projections of the quartz and plagioclase grains (one-point-per-grain). (o) Quartz grain boundaries. (p) Plagioclase grain*

boundaries. (q) Quartz-Plagioclase phase boundaries. Each equal-area projection is contoured to multiples of uniform density (MUD); the minimum and maximum values are at the bottom and top of the vertical bars, respectively. The yellow boxes in the equal-area projections denote points of maximum intensity. The R values indicate the degree of randomness of each c-axis distribution (Vollmer, 1990). The 'bilbao' colour map of Crameri (2018) is used here. N_g: number of grains. Empty square, circle, and triangle markers correspond to the grain and phase boundaries of maps (a), (f) and (m), respectively. Mineral abbreviations are as per Whitney and Evans (2010).

5. Discussion

5.1. Phase-specific deformation mechanisms

Inside the shear bands, quartz grains constitute either the recrystallised matrix or the monomineralic ribbons. They exhibit prominent undulose extinction in the latter, implying intracrystalline plasticity. The layered structure of SB1 is conspicuous, with quartz ribbons alternated by the interconnected weaker matrix of recrystallised quartz and feldspar grains (**Fig. 2a**). Albeit less prominent, SB2 also exhibits a similar layered structure near its margins (**Fig. 7b**). In contrast, SB3 lacks such alternation and K-feldspar, instead of plagioclase, forms the load-bearing framework (**Fig. 7c**). Although the deformation-induced layered fabric is common for mylonitic granites/polyphase rocks (Berthé et al., 1979; Handy, 1990; Tremblay and Malo, 1991; Schulmann et al., 1996), their absence may indicate early stages or weaker degree of mylonitisation (e.g., Park et al., 2006). Moreover, the dominant deformation mechanisms in such cases can differ from one layer to another (e.g., Behrmann and Mainprice, 1987; Kruse and Stünitz, 1999; Ribeiro et al., 2019). Below, we discuss in detail the mechanisms by which the deformation of the studied shear bands was accommodated by the quartz and feldspar (plagioclase and K-feldspar) grains.

5.1.1. Quartz

The quartz grains in the quartz-rich domains of the shear bands are devoid of microfractures, suggesting that they accommodated strain in the viscoplastic regime. The boundaries of quartz grains constituting the ribbons exhibit prominent bulges (**Figs. 2h, i**). They are larger than the bulges produced via slow grain boundary migration (Stipp et al., 2002). Therefore, fast grain boundary migration and similar subgrain size (**Figs. 2g-i**), like the nearby recrystallised grains, testify for SGR (subgrain rotation) recrystallisation (Stipp et al., 2002), respectively. Intragranular deformation and subgrain formation in the quartz grains, both within (quartz ribbons) and adjacent to the shear bands, is also clearly depicted in the mis2mean maps (**Fig. 11**). The stepwise increments of the point-to-origin misorientation values, along the line profiles, from the cores to the rims of the quartz grains confirm SGR recrystallisation mechanism (Halfpenny et al., 2006), which is also supported by the clustered arrangement of the quartz grain boundaries (**Fig. 12m**) (Heilbronner and Barrett, 2014). The quartz CPOs in SB1 (**Fig. 8a**) and SB2 (**Fig. 8c**) also exhibit point and girdle distributions and support their deformation via dislocation creep processes. The number of quartz grains in SB3 is significantly lower than that in SB1 and SB2; consequently, we refrain from drawing inferences about the deformation mechanism from the corresponding CPOs. The higher degree of misfit between the uncorrelated and theoretical MADs, compared to that of the feldspars, suggests relatively stronger intracrystalline deformation (**Figs. 9a, c**). Although the mean correlated misorientations, calculated for misorientations ≥10° (i.e., neighbouring 'grains'), are high (~50°), the high misfits between the correlated and theoretical MADs (**Figs. 9a, c**), as well as the ordered nature of the high-angle MXDs (Figs. 9a, c), suggest crystal plastic deformation must

have affected the quartz grains. If GBS mechanism were active, it was either negligible or non-rotational (Wheeler et al., 2001; Lapworth et al., 2002).

SB1 and SB2 also contain a separate set of quartz grains in the plagioclase-rich domains, which are products of the myrmekitisation that proceeded by the reaction shown below (Phillips et al., 1972).

$$\left\{\begin{matrix} 3x\mathrm{KAlSi_3O_8} \\ y\mathrm{NaAlSi_3O_8} \\ z\mathrm{Ca_{\square}(AlSi_3O_8)_2} \end{matrix}\right\} + x\mathrm{H_2O} \rightarrow x\mathrm{KAl_2(Al,Si_3)O_{10}(OH)_2} + \left\{\begin{matrix} y\mathrm{NaAlSi_3O_8} \\ z\mathrm{CaAl_2Si_2O_8} \end{matrix}\right\} + (6x+4z)\mathrm{SiO_2} + x\mathrm{K_2O}$$

alkali feldspar water muscovite $\underbrace{\text{plagioclase}\quad\quad\text{quartz}}_{\text{myrmekite}}$ … (1)

$\square$ *implies vacant cation sites*, $x > y \gg z$.

These quartz grains do not constitute the ribbons but occur at the triple junctions of recrystallised plagioclase grains (**Figs. 12a, f, l**). The anti-clustered distributions of the phase boundaries at regions away from quartz ribbons in SB1 (**Supplementary Figs. SF6a, e**) and around the K-feldspar porphyroclast in SB2 (**Figs. 12a, e, f, j**) are also suggestive of heterogeneous nucleation (Heilbronner and Barrett, 2014) commonly associated with myrmekitisation (Ceccato et al., 2018). Continued reaction-induced heterogeneous nucleation promoted phase mixing, which in turn impeded the grains from growing and allowed switching to GBS accommodated by GBD (Fliervoet et al., 1997; Kilian et al., 2011; Czaplińska et al., 2015). The corresponding quartz CPOs (**Figs. 8b, d, 12b, g**) are also much weaker than those from the domains rich in quartz ribbons (**Figs. 8a, c, 12n**) exhibiting clustered phase and grain boundaries (**Figs. 12k, o-q**), implying the dominance of GSS creep mechanism in the former compared to dislocation creep activity in the latter.

All these observations point that dislocation creep and dynamic recrystallisation by SGR mechanism were pivotal in accommodating the deformation of quartz grains in the ribbons,

whereas the finer quartz grains, products of dynamic recrystallisation and myrmekitisation, deformed by GSS creep. GBS, in the case of the latter, if any, was non-rotational and, therefore, could not destroy the systematic arrangement of the high-angle MXDs (**Fig. 10**).

5.1.2. Plagioclase and K-feldspar

Brittle fracturing of the feldspar grains, although more prominent outside/adjacent to the shear bands, is also evident from the angular habits of the isolated porphyroclasts within the shear bands (**Figs. 4c-f**) and are most likely to be the remnants of the cataclasis that facilitated shear band nucleation and generated the isolated porphyroclasts. Apart from the formation of the porphyroclasts, a second phase of grain size reduction (cf. Zhou et al., 2022) process were active and BLG mechanism produced daughter feldspar grains (both plagioclase and K-feldspar) in the shear bands, which are extremely fine in size (median equivalent grain diameters SB1: 24 microns, SB2: 21 microns, SB3: 28 microns), suitable for GSS creep (Tullis, 1990; Stünitz and Fitz Gerald, 1993; Rybacki and Dresen, 2004). The feldspar grains also exhibit equant shapes (**Fig. 5a**), straight boundaries (**Fig. 5b**), hourglass shape (**Fig. 5c**), and quadruple intersections (**Fig. 5d**), all of which signify the Lifshitz GBS mechanism (Langdon, 1991, 1993, 2006; Ree, 1994; Lapworth et al., 2002; Maruyama and Hiraga, 2017).

The plagioclase CPOs in SB1 and SB2 are weak (**Figs. 8a-d**) in both quartz-rich and plagioclase-rich domains, whereas those of SB3 are relatively stronger (**Fig. 8e**), which could be due to the fewer number of grains (171 compared to 462 and 755 in SB1 and 1054 and 1846 in SB2). The uncorrelated MADs are also nearly equivalent to the theoretical random distributions in all the shear bands (**Fig. 9**). Moreover, none of the CPOs suggests the dominance of slip on (010), the most easily activated slip plane in plagioclase due to dislocation creep deformation (Ji

and Mainprice, 1990; Kruse et al., 2001). Plagioclase CPO distributions within the different domains across SB1 and SB2 also vary with respect to the kinematic reference frame (**Supplementary Fig. SF7**). These observations indicate that either the CPOs are products of diffusion creep (Jiang et al., 2000; Wheeler et al., 2001) and/or the dislocation creep-induced CPOs were randomised due to subsequent GBS (Zhang et al., 1994; Pearce et al., 2011; Soda et al., 2019). In all the shear bands, the low-angle (2-10°) misorientation axes of plagioclase grains exhibit strong and preferred orientations in the crystal coordinate system, with the maxima girdles being nearly parallel to (010) (**Fig. 9**). Such crystallographically controlled distributions of the low-angle misorientation axes along with the high frequency of the correlated MADs in 2-10° intervals (**Fig. 9**) are clear indications of remnant intragranular strain by dislocation glide (e.g., Díaz Aspiroz et al., 2007). The weak CPOs (**Figs. 8a-d**), high (>100°) mean misorientation, calculated only for ≥10° misorientations (i.e., neighbouring 'grains') (**Fig. 9**), the low misfit between the correlated and uncorrelated MADs with the latter being identical to the theoretical MADs (**Fig. 9**), and weak preferred orientations of the high-angle (40-160°) misorientation axes (**Fig. 10**) are all suggestive of GBS mechanism (Fliervoet et al., 1997; Jiang et al., 2000; Bestmann and Prior, 2003). The fine grain size of plagioclase in the shear bands also supports deformation in the GSS creep regime, in which GBS commonly dominates (Kenkmann and Dresen, 2002; Platt, 2015; Zuza et al., 2022).

We have also noted that the coarse plagioclase grains adjacent to and outside SB3 exhibit stronger CPOs, greater misfit between uncorrelated and theoretical MADs, and more preferred axis distributions for both low (2-10°) and high (>40°) misorientations angles (**Supplementary Fig. SF8**), than the finer grains present within the shear bands, suggestive of intense

intragranular deformation due to dislocation creep. We propose that the fine-grained plagioclase aggregates inside the shear bands originated due to the comminution of parent porphyroclasts and accommodated deformation by GBS as the shear bands developed. Consequently, these finer plagioclase grains preserve partial signatures of the prior dislocation creep activity, e.g., many low-angle boundaries and crystallographically controlled low-angle misorientation axes (**Fig. 9**) that affected the porphyroclasts. Subsequently, GBS weakened the strong CPO that the daughter plagioclase grains inherited from their parent porphyroclasts. The results of the phase spatial distribution analysis (Sec. 4.3.4.) demonstrate random and nearly random distributions for the plagioclase grain contacts. It confirms the possibility of GBS (Heilbronner and Barrett, 2014).

The shear bands contain another category of fine plagioclase grains around the K-feldspar porphyroclasts, which originated due to myrmekitisation (**Fig. 13a**) (Eqn. 1 in Sec. 5.1.1). The progress of the reaction front into the K-feldspar porphyroclast is also evident in the thin-section (**Fig. 3b**). The presence of myrmekites is often attributed to deformation of the K-feldspar by dissolution precipitation creep (e.g., Ceccato et al., 2018), which is further confirmed from the film-like amorphous feldspar precipitates along with spheroidal/cylindrical crystallites on feldspar grain surfaces (Fusseis et al., 2009) visible in the broken surface SEM images (**Figs. 6b, c**). The CPOs of quartz, plagioclase, and K-feldspar grains from the vicinity of a K-feldspar porphyroclast in SB2 (**Fig. 13b**) support the topotactic replacement commonly reported as myrmekitisation product (Ceccato et al., 2018; Song et al., 2021), e.g., the parallelism between distributions of K-feldspar (001), (100), (010), (20-1), [001], and [100] to the corresponding CPO plots of plagioclase grains. Additional topotactic relationships are also

observed between K-feldspar and quartz CPOs: $(001)_{Kfs}$ || $\{10\text{-}12\}_{Qz}$, $(100)_{Kfs}$ || $\{20\text{-}21\}_{Qz}$, $(010)_{Kfs}$ || $\{10\text{-}11\}_{Qz}$, and $(20\text{-}1)_{Kfs}$ || $\{11\text{-}21\}_{Qz}$, and between plagioclase and quartz CPOs: $(001)_{Pl}$ || $\{10\text{-}11\}_{Qz}$, $(100)_{Pl}$ || $\{11\text{-}21\}_{Qz}$, $(110)_{Pl}$ || $\{10\text{-}12\}_{Qz}$, and $(110)_{Pl}$ || $\{20\text{-}21\}_{Qz}$ (**Fig. 13b**). Nearly similar distributions of correlated and theoretical misorientations (**Fig. 13c**) imply that deformation of these plagioclase grains was particularly followed by GBS after they were generated as reaction product (Wheeler et al., 2001). Although such arrangements of plagioclase and quartz grains surrounding K-feldspar porphyroclasts are also present in SB1 (**Supplementary Fig. SF9**), EBSD data was collected only from SB2.

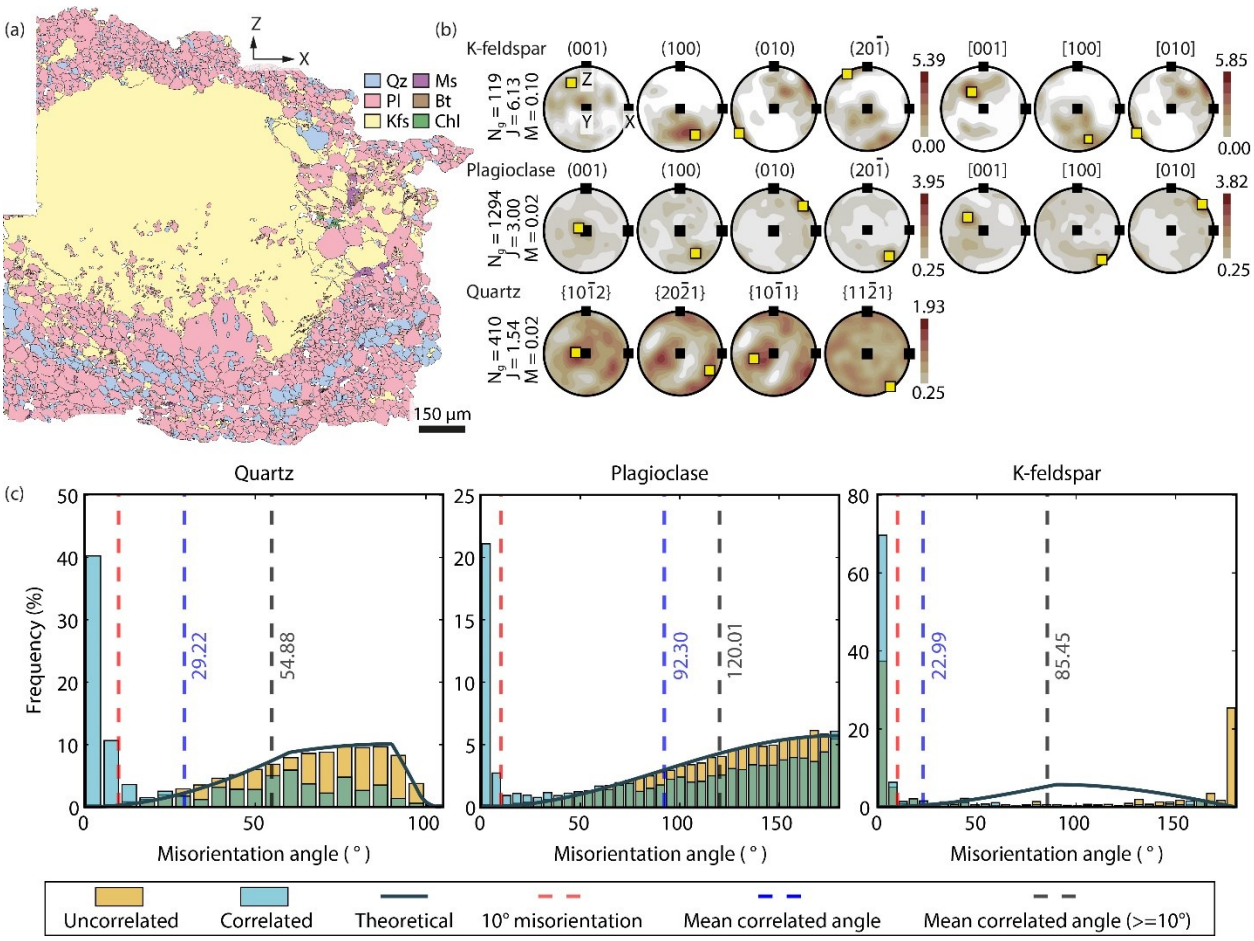

Fig. 13. *Myrmekitisation and CPO inheritance. (a) Phase map of the region of interest. (b) Equal-area projections (one-point-per-grain) of the CPOs of K-feldspar, plagioclase, and quartz grains. Each equal-area projection is contoured to multiples of uniform density (MUD); the minimum and maximum values are at the bottom and top of the vertical bars, respectively. The yellow boxes denote points of maximum intensity. Ng: number of grains, J: J-Index (Bunge, 1982), and M: M-Index (Skemer et al., 2005). The 'bilbao' colour map of Crameri (2018) is used here. (c) Misorientation angle distributions of the phases. The red dashed lines mark the 10° misorientation. The blue and black dashed lines indicate the mean misorientation angles of the correlated distributions considering ≥2° and ≥10° misorientations, respectively.*

Overall, the K-feldspar grains in SB1 and SB2 are sparse; therefore, we do not comment on the deformation intensities from their CPOs. The K-feldspar CPO distributions in SB3 are random. None of them is consistent with the slip system activities commonly expected for K-feldspar grains deformed naturally via dislocation creep, e.g., (010)[001], (010)[100], or

(010)[101] (Sacerdoti et al., 1980; Schulmann et al., 1996; Ishii et al., 2007). But the low-angle MXDs of K-feldspar grains in all three shear bands show strongly concentrated distributions around [001] and [010], with the former being dominant (**Fig. 9**). Assuming tilt nature for the low-angle boundaries in K-feldspar grains, the low-angle MXDs suggest the dominance of (100)[010] slip system activity along with minor contributions from that of the (100)[001] or (001)[100] slip systems (see fig. 2a of Dutta et al., 2022). The MADs and MXDs (**Fig. 9**) for the K-feldspar grains in the three shear bands indicate many low-angle boundaries suggestive of possible dislocation creep deformation. However, the low-to-negligible misfits between the uncorrelated and theoretical MADs of K-feldspar grains in SB3 (**Fig. 9e**) imply minimal intragranular deformation (Wheeler et al., 2001). These observations suggest that the finer K-feldspar grains, like the plagioclase grains, also originated by comminution of the more deformed parent porphyroclasts. However, the mean misorientation, calculated without <10° misorientations (i.e., neighbouring 'grains') (**Figs. 9a-c, e**), for the corresponding K-feldspar grains in the three shear bands, are high, though not as high as the plagioclase grains. In addition, the distributions of the axes corresponding to high-angle misorientations (40-160°) are more systematic compared to that of plagioclase (**Fig. 10**). Collectively, these results demonstrate that the finer K-feldspar grains, like the plagioclase grains, also experienced rotational GBS that randomised (**Fig. 8e**) the pre-existing CPO inherited from the parent porphyroclast (e.g., Lapworth et al., 2002). But the rotational component in the case of the K-feldspar grains was probably lesser compared to the plagioclase grains and resulted in a relatively more systematic arrangement of the high-angle misorientation axes in the former (**Fig. 10**).

5.2. Deformation temperature

As discussed earlier, the quartz grains in the shear bands are devoid of microfractures and exhibit evidence of SGR recrystallisation mechanism (**Fig. 2**), implying deformation temperatures in the range of 400-500°C (Stipp et al., 2002). Additionally, flame perthites and myrmekitic texture in the feldspar grains (**Fig. 3**) indicate that the temperature was 400-500°C (Simpson and Wintsch, 1989; Pryer and Robin, 1995; Passchier and Trouw, 2005). The low-angle MXDs of the quartz grains from all the shear bands (**Fig. 9**) indicate a dominance of prism-áañ slip-system activity, which confirms the temperature range mentioned above (Wilson, 1975; Schmid and Casey, 1986; Précigout et al., 2022). Although rare, dislocation glide and slip system activity in K-feldspar grains can occur at 400-500°C (Sacerdoti et al., 1980; Fitz Gerald and Stünitz, 1993). In Sec. 5.1.2. Plagioclase and K-feldspar, we pointed out the possibility of (100)[010] slip system activity in the K-feldspar grains in all three shear bands. The (100)[010] slip system is reported for K-feldspar grains deformed at 400-500°C, mid-to-upper greenschist facies (Ishii et al., 2007; Viegas et al., 2014). Therefore, it is reasonable to infer that neither of the shear bands experienced temperatures > 500°C.

5.3. Fluid influx

Fractures in the feldspar porphyroclasts from the host granite adjacent to SB1 (**Fig. 4a**), filled with finer fragments of porphyroclasts (Okudaira et al., 2015, 2017), increase the permeability of the fluid. The continuity of the fractures forming channels away from the shear bands (**Figs. 4a, b**) is prominent, and as such, fluid infiltration along the brittle precursor of the shear band seems plausible (e.g., Gardner et al., 2021). Moreover, the presence of sub-rounded, isolated feldspar porphyroclasts within the shear bands (**Figs. 4c-f**) also hints at the

cataclastic origin of these porphyroclasts (e.g., Wintsch and Yeh, 2013). Cataclasis and fracturing in rocks preferentially initiate along weaker zones, which could be foliation-parallel, and facilitate fluid infiltration as well as transport (Kronenberg et al., 1990; Magloughlin, 1992; Holdsworth et al., 2001; Kawano et al., 2011; Sullivan and Monz, 2016). Within the studied shear bands, the biotite and chlorite grains are arranged in the form of anastomosing thread-like networks running parallel to the shear band margins (**Figs. 1e, g, i**) and deflecting around the recrystallised grains (**Fig. 5f**), suggesting that their fluid-assisted precipitation along pre-existing weak planes was syn-kinematic (Graziani et al., 2020). Although less abundant, such fluid-derived phyllosilicate-rich networks also occur outside the shear bands. Their preferential arrangement, particularly prominent in the samples S1 and S2, outside and adjacent to SB1 (**Fig. 1e**) and SB2 (**Fig. 1g**), respectively, attests to the overall sinistral shearing, also exhibited by the quartz and plagioclase grains from within the shear bands (SPOs in **Figs. 7d-f**). These findings suggest that following cataclastic comminution of the granite, fluids invaded the zone of reduced grain size, anastomosed around the finer grains, and caused shear to localise in the thin bands. The fluids also permeated the regions adjacent to the bands along intergranular spaces and fractures (**Figs. 4a, b**). The coalescence of crystallographically controlled pores on the quartz grain surfaces (**Fig. 6a**) implies that the granular fluid pumping mechanism was also active along the grain boundaries (Fusseis et al., 2009). The granular fluid pumping mechanism ensures the maintenance of dynamic equilibrium of the pore pressures at the grain junctions, consequently nullifying the requirement of additional pressure gradients for the fluid to permeate the incipient shear band successfully. Notably, granular fluid pumping and subsequent sustenance of pore pressure equilibrium are possible if creep cavitation induced by

diffusion-accommodated grain boundary sliding is operative (Fusseis et al., 2009). We confirmed GBS activity in the studied shear bands using thin-section, broken surface SEM, and EBSD-derived observations (Sec. 5.1).

5.4. Shear band evolution schemata

Our observations suggest that the origin and development of the shear bands within the pink granite of the Bundelkhand Craton occurred at temperatures <500°C (Sec. 5.2), which is also the upper limit for brittle-ductile transitional behaviour of granites (Passchier, 1984; Simpson, 1985; Guermani and Pennacchioni, 1998). Although the peak deformation temperature experienced by the granite prior to shear band formation is unavailable, strong intragranular deformation of plagioclase grains from the host (**Supplementary Fig. SF8**) confirms that the temperature was high enough (>500°C) for dislocation creep deformation of feldspar grains. Geochemical proxies established that the granitic batholith of BGGC experienced significant unroofing (Absar et al., 2009). Subsequent brittle fracturing due to residual stresses (Absar et al., 2009; Nadan and Engelder, 2009) at a later stage of exhumation of the granite created instabilities along which the shear bands nucleated (**Fig. 14a**). Comminution of the stronger feldspar grains/porphyroclasts increased the permeability and concomitant fluid influx allowed deformation to localise within the incipient shear bands (**Figs. 14b, c**). Semi-brittle flow characterised the overall deformation of the quartzo-feldspathic shear bands that ensued, and as such, the quartz and feldspar grains deformed in ductile and brittle regimes, respectively (**Fig. 14d**) (Mitra, 1978; Evans et al., 1990; Passchier and Trouw, 2005). The finer quartz grains originated by dislocation creep processes, i.e., dynamic recrystallisation via SGR and as products of myrmekitisation, i.e., dissolution-precipitation creep, of the K-

feldspar porphyroclasts (**Fig. 14e**) (e.g., Menegon et al., 2008). Whereas the feldspar grains undergoing an initial grain size diminution by cataclasis, faced crystal plastic deformation via diffusion creep, and fine granulation was mainly accomplished by BLG recrystallisation. Some of the fine plagioclase grains were also produced during myrmekitisation (Sec. 5.1). Nevertheless, the extreme grain size reduction was instrumental in switching the deformation accommodating mechanism from GSI creep to GSS creep (Etheridge and Wilkie, 1979; Stünitz and Fitz Gerald, 1993; Kilian et al., 2011) and favoured GBS (**Fig. 14d**). Syn-kinematic fluid infiltration and GBS (Sec. 5.3) acted in tandem to ensure superplastic flow within the shear bands (**Fig. 14f**). Fluid films along the grain boundaries facilitated GBS (Tullis and Yund, 1991; Tullis et al., 1996), minimised intragranular deformation, thereby guiding the overall recrystallisation processes within the granite shear bands. Due to minimal intragranular deformation post-grain size reduction, plagioclase and K-feldspar grains preserve remnants of the dislocation creep activities, which their respective parent crystals experienced before the shear band nucleation.

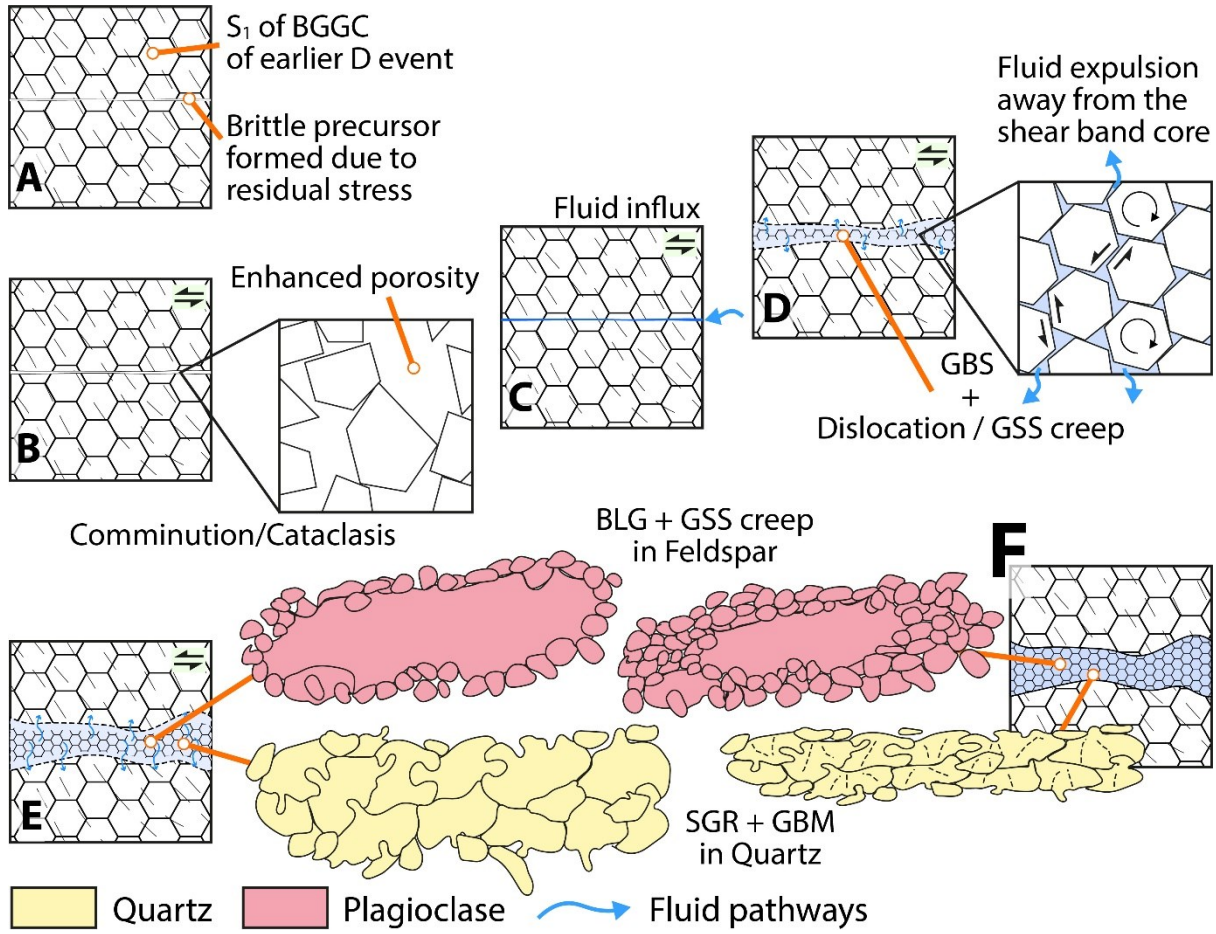

Fig. 14. *A schematic illustration showing different stages of the shear band evolution in the BGGC. (a) Early stages of deformation prior to shear band localisation. (b) The onset of shear band localisation is marked by brittle fracturing. (c) Increased permeability allowed fluid influx. (d) The quartz and feldspar deformed selectively. (e) The later stage of shear band evolution, where the band widens laterally. (f) The final stage, i.e., present state of the shear bands. Dashed lines inside quartz grains are schematic subgrain boundaries.*

6. Conclusions

Deformation mechanisms at a particular P-T condition depend on phase rheologies. To assess this, we studied three ductile shear bands of different thicknesses (SB1: 3.3 mm, SB2: 4.4 mm, SB3: 0.8 mm) from three granite samples with dissimilar phase distributions and unusually high shear strain (SB1: 16.2, SB2: 23.9, SB3: 37.3). These shear bands nucleated along brittle precursors. Grain size reduction due to cataclasis of the feldspar porphyroclasts and dynamic

recrystallisation of the quartz and feldspar grains, along with fluid infiltration, localised the deformation and contributed to the growth of the shear bands. The finer grain size facilitated GSS creep. Aqueous fluid presence facilitated myrmekitic bands of fine-grained plagioclase, mimicking the CPOs of their parent K-feldspar grains. Isolated quartz grains, also produced from myrmekitisation, occupy the triple junctions of these plagioclase grains. Such arrangements of plagioclase and quartz grains impeded their growth due to pinning and ensured deformation by GSS creep. Fluid-assisted GBS effectively weakened the CPOs and randomised the high-angle (>40°) misorientation axes, though plagioclase grains were affected more than quartz and K-feldspar grains. The relatively coarser quartz grains constituting the monomineralic bands deformed via dislocation creep, whereas the finer plagioclase and K-feldspar grains deformed by Lifshitz GBS. Despite negligible intragranular deformation, the high frequencies of subgrain boundaries in K-feldspar and plagioclase grains could be remnants of dislocation creep activity prior to shear band formation. Albeit having low intracrystalline plasticity and equidimensional grain habits, the studied shear bands exhibit high ductile strain, evident from the torn quartz ribbons inside the shear bands and their shear plane parallel orientations. Accommodation of high shear strain inside narrow shear bands cannot be achieved solely by crystal plastic deformation. Therefore, we propose that superplastic deformation by GBS of the finer fractions of quartz and feldspar grains accommodated the additional strain. Our study demonstrates that superplasticity can operate in naturally deformed, mid-crustal granitic shear bands with a median grain size of 20-30 microns.

Appendix

The shear strain of SB1, SB2 and SB3 are calculated with the assumption of simple shear deformation and throughout the event, the function (Pennacchioni and Mancktelow, 2018):

$$d = \int_0^t \gamma \, dt \quad \text{… (A1)}$$

was continuous. The thickness, *t* and displacement, *d* is measured from field photographs. Displacement *d* is measured from mid-point to mid-point of the marker veins. The *d* values are 53.5, 105.4 and 29.8 mm for SB1, SB2 and SB3. The *t* values are 3.3, 4.4 and 0.8 mm (measured from the thin sections), respectively. The γ of the shear bands are 16.2, 23.9 and 37.9. The finite shear strain γ and the quadratic elongation (λ) can be written as (Rybacki et al., 2003),

$$\lambda = \frac{1}{2}(\gamma^2 + 2 + \gamma\sqrt{\gamma^2 + 4}) \ . \quad \text{… (A2)}$$

We know,

$$s = \sqrt{\lambda} \quad \text{… (A3)}$$

This method gives us the *s* values, 1626%, 2394% and 3732% for SB1, SB2 and SB3, respectively (**Supplementary Fig. SF1**).

Acknowledgements

We thank Toru Takeshita for handling the editorial processes and the two anonymous reviewers for thoroughly reviewing the manuscript. The EBSD data acquisition was facilitated by the technicians from the Advanced Center for Material Science (ACMS) at IIT Kanpur. AS and DD acknowledge the support of the Prime Minister's Research Fellowship (Govt. of India) and the IIT Kanpur Postdoctoral Fellowship. This work is part of the Swarnajayati Fellowship (DST/SJF/EASA-01/2015-16) awarded to SM.

Data Statement

The EBSD data used in this study can be obtained from the Mendeley Data Repository (https://data.mendeley.com/datasets/xjyf878w3n/2).

References

Absar, N., Raza, M., Roy, M., Naqvi, S.M., Roy, A.K., 2009. Composition and weathering conditions of Paleoproterozoic upper crust of Bundelkhand craton, Central India: Records from geochemistry of clastic sediments of 1.9Ga Gwalior Group. Precambrian Research 168, 313–329. https://doi.org/10.1016/j.precamres.2008.11.001

Alaoui, K., Airaghi, L., Dubacq, B., Rosenberg, C.L., Bellahsen, N., Précigout, J., 2023. Role of pre-kinematic fluid-rock interactions on phase mixing, quartz recrystallization and strain localization in low-temperature granitic shear zones. Tectonophysics 850, 229735. https://doi.org/10.1016/j.tecto.2023.229735

Barraud, J., 2006. The use of watershed segmentation and GIS software for textural analysis of thin sections. Journal of Volcanology and Geothermal Research, Modern Trends in Petrography: 154, 17–33. https://doi.org/10.1016/j.jvolgeores.2005.09.017

Basu, A., 1986. Geology of parts of the Bundelkhand Craton, central India. Rec. Geol. Surv. India 101, 61–124.

Behrmann, J.H., 1985. Crystal plasticity and superplasticity in quartzite; A natural example. Tectonophysics 115, 101–129. https://doi.org/10.1016/0040-1951(85)90102-7

Behrmann, J.H., Mainprice, D., 1987. Deformation mechanisms in a high-temperature quartz-feldspar mylonite: evidence for superplastic flow in the lower continental crust. Tectonophysics 140, 297–305. https://doi.org/10.1016/0040-1951(87)90236-8

Bercovici, D., Skemer, P., 2017. Grain damage, phase mixing and plate-boundary formation. Journal of Geodynamics 108, 40–55. https://doi.org/10.1016/j.jog.2017.05.002

Berthé, D., Choukroune, P., Jegouzo, P., 1979. Orthogneiss, mylonite and non coaxial deformation of granites: the example of the South Armorican Shear Zone. Journal of Structural Geology 1, 31–42. https://doi.org/10.1016/0191-8141(79)90019-1

Bestmann, M., Prior, D.J., 2003. Intragranular dynamic recrystallization in naturally deformed calcite marble: diffusion accommodated grain boundary sliding as a result of subgrain rotation recrystallization. Journal of Structural Geology 25, 1597–1613. https://doi.org/10.1016/S0191-8141(03)00006-3

Bhattacharya, A.R., Singh, S.P., 2013. Proterozoic crustal scale shearing in the Bundelkhand massif with special reference to quartz reefs. Journal of the Geological Society of India 82, 474–484. https://doi.org/10.1007/s12594-013-0178-4

Boullier, A.M., Gueguen, Y., 1975. SP-Mylonites: Origin of some mylonites by superplastic flow. Contributions to Mineralogy and Petrology 50, 93–104. https://doi.org/10.1007/BF00373329

Bunge, H.-J., 1982. Texture Analysis in Materials Science: Mathematical Methods. Butterworth-Heinemann, Butterworths, London.

Ceccato, A., Menegon, L., Pennacchioni, G., Morales, L.F.G., 2018. Myrmekite and strain weakening in granitoid mylonites. Solid Earth 9, 1399–1419. https://doi.org/10.5194/se-9-1399-2018

Chokshi, A.H., Mukherjee, A.K., Langdon, T.G., 1993. Superplasticity in advanced materials. Materials Science and Engineering: R: Reports 10, 237–274. https://doi.org/10.1016/0927-796X(93)90009-R

Crameri, F., 2018. Scientific colour maps. https://doi.org/10.5281/ZENODO.1243862

Czaplińska, D., Piazolo, S., Zibra, I., 2015. The influence of phase and grain size distribution on the dynamics of strain localization in polymineralic rocks. Journal of Structural Geology 72, 15–32. https://doi.org/10.1016/j.jsg.2015.01.001

Dey, S., Moyen, J.-F., 2020. Archean granitoids of India: windows into early Earth tectonics – an introduction. In: Dey, S., Moyen, J.-F. (Eds.), Archean Granitoids of India: Windows into Early Earth Tectonics. Geological Society London, Special Publications, 1–13.

Díaz Aspiroz, M., Lloyd, G.E., Fernández, C., 2007. Development of lattice preferred orientation in clinoamphiboles deformed under low-pressure metamorphic conditions. A SEM/EBSD study of metabasites from the Aracena metamorphic belt (SW Spain). Journal of Structural Geology 29, 629–645. https://doi.org/10.1016/j.jsg.2006.10.010

Dimanov, A., Rybacki, E., Wirth, R., Dresen, G., 2007. Creep and strain-dependent microstructures of synthetic anorthite–diopside aggregates. Journal of Structural Geology 29, 1049–1069. https://doi.org/10.1016/j.jsg.2007.02.010

Drury, M.R., Avé Lallemant, H.G., Pennock, G.M., Palasse, L.N., 2011. Crystal preferred orientation in peridotite ultramylonites deformed by grain size sensitive creep, Étang de Lers, Pyrenees, France. Journal of Structural Geology 33, 1776–1789. https://doi.org/10.1016/j.jsg.2011.10.002

Dutta, D., Misra, S., Karmakar, S., 2022. Deformation mechanisms and characteristics of the meta-BIFs from an early Proterozoic shear system of the Southern Granulite Terrane (SGT), India. Journal of Structural Geology 156, 104534. https://doi.org/10.1016/j.jsg.2022.104534

Edington, J.W., Melton, K.N., Cutler, C.P., 1976. Superplasticity. Progress in Materials Science 21, 61–170. https://doi.org/10.1016/0079-6425(76)90005-0

Etheridge, M.A., Wilkie, J.C., 1979. Grainsize reduction, grain boundary sliding and the flow strength of mylonites. Tectonophysics 58, 159–178. https://doi.org/10.1016/0040-1951(79)90327-5

Evans, B., Fredrich, J.T., Wong, T., 1990. The brittle-ductile transition in rocks: Recent experimental and theoretical progress. In: Duba, A.G., Durham, W.B., Handin, J.W., Wang, H.F. (Eds.), The Brittle-Ductile Transition in Rocks, Geophysical Monograph Series. American Geophysical Union, Washington, D. C., 1–20. https://doi.org/10.1029/GM056p0001

Fitz Gerald, J.D., Stünitz, H., 1993. Deformation of granitoids at low metamorphic grade. I: Reactions and grain size reduction. Tectonophysics 221, 269–297. https://doi.org/10.1016/0040-1951(93)90163-E

Fliervoet, T.F., White, S.H., Drury, M.R., 1997. Evidence for dominant grain-boundary sliding deformation in greenschist- and amphibolite-grade polymineralic ultramylonites from the Redbank Deformed Zone, Central Australia. Journal of Structural Geology 19, 1495–1520. https://doi.org/10.1016/S0191-8141(97)00076-X

Fusseis, F., Regenauer-Lieb, K., Liu, J., Hough, R.M., De Carlo, F., 2009. Creep cavitation can establish a dynamic granular fluid pump in ductile shear zones. Nature 459, 974–977. https://doi.org/10.1038/nature08051

Gardner, J., Wheeler, J., Mariani, E., 2021. Interactions between deformation and dissolution-precipitation reactions in plagioclase feldspar at greenschist facies. Lithos 396–397, 106241. https://doi.org/10.1016/j.lithos.2021.106241

Gilotti, J.A., Hull, J.M., 1990. Phenomenological superplasticity in rocks. In: Knipe, R.J., Rutter, E.H. (Eds.), Deformation Mechanisms, Rheology and Tectonics. Geological Society of London Special Publications 54, 229–240. https://doi.org/10.1144/GSL.SP.1990.054.01.22

Graziani, R., Larson, K.P., Soret, M., 2020. The effect of hydrous mineral content on competitive strain localization mechanisms in felsic granulites. Journal of Structural Geology 134, 104015. https://doi.org/10.1016/j.jsg.2020.104015

Guermani, A., Pennacchioni, G., 1998. Brittle precursors of plastic deformation in a granite: an example from the Mont Blanc massif (Helvetic, western Alps). Journal of Structural Geology 20, 135–148. https://doi.org/10.1016/S0191-8141(97)00080-1

Halfpenny, A., Prior, D.J., Wheeler, J., 2006. Analysis of dynamic recrystallization and nucleation in a quartzite mylonite. Tectonophysics 427, 3–14. https://doi.org/10.1016/j.tecto.2006.05.016

Handy, M.R., 1990. The solid-state flow of polymineralic rocks. Journal of Geophysical Research: Solid Earth 95, 8647–8661. https://doi.org/10.1029/JB095iB06p08647

Heilbronner, R., Barrett, S., 2014. Spatial Distributions. In: Heilbronner, R., Barrett, S. (Eds.), Image Analysis in Earth Sciences: Microstructures and Textures of Earth Materials. Springer, Berlin, Heidelberg, 351–368. https://doi.org/10.1007/978-3-642-10343-8_18

Heilbronner, R., Barrett, S., 2013. Image Analysis in Earth Sciences: Microstructures and Textures of Earth Materials. Springer Science & Business Media.

Hielscher, R., Schaeben, H., 2008. A novel pole figure inversion method: specification of the MTEX algorithm. Journal of Applied Crystallography 41, 1024–1037. https://doi.org/10.1107/S0021889808030112

Holdsworth, R.E., Stewart, M., Imber, J., Strachan, R.A., 2001. The structure and rheological evolution of reactivated continental fault zones: a review and case study. In: Miller, J.A., Holdsworth, R.E., Buick, I.S., Hand, M. (Eds.), Continental Reactivation and Reworking. Geological Society of London, Special Publications 184, 115–137. https://doi.org/10.1144/GSL.SP.2001.184.01.07

Imon, R., Okudaira, T., Fujimoto, A., 2002. Dissolution and precipitation processes in deformed amphibolites: an example from the ductile shear zone of the Ryoke metamorphic belt, SW Japan. Journal of Metamorphic Geology 20, 297–308. https://doi.org/10.1046/j.1525-1314.2002.00367.x

Ishii, K., Kanagawa, K., Shigematsu, N., Okudaira, T., 2007. High ductility of K-feldspar and development of granitic banded ultramylonite in the Ryoke metamorphic belt, SW Japan. Journal of Structural Geology 29, 1083–1098. https://doi.org/10.1016/j.jsg.2007.02.008

Ji, S., Mainprice, D., 1990. Recrystallization and Fabric Development in Plagioclase. The Journal of Geology 98, 65–79.

Jiang, Z., Prior, D.J., Wheeler, J., 2000. Albite crystallographic preferred orientation and grain misorientation distribution in a low-grade mylonite: implications for granular flow. Journal of Structural Geology 22, 1663–1674. https://doi.org/10.1016/S0191-8141(00)00079-1

Joshi, K.B., Bhattacharjee, J., Rai, G., Halla, J., Ahmad, T., Kurhila, M., Heilimo, E., Choudhary, A.K., 2017. The diversification of granitoids and plate tectonic implications at the

Archaean–Proterozoic boundary in the Bundelkhand Craton, Central India. Geological Society, London, Special Publications 449, 123–157. https://doi.org/10.1144/SP449.8

Kaur, P., Zeh, A., Chaudhri, N., Eliyas, N., 2016. Unravelling the record of Archaean crustal evolution of the Bundelkhand Craton, northern India using U–Pb zircon–monazite ages, Lu–Hf isotope systematics, and whole-rock geochemistry of granitoids. Precambrian Research 281, 384–413. https://doi.org/10.1016/j.precamres.2016.06.005

Kawano, S., Katayama, I., Okazaki, K., 2011. Permeability anisotropy of serpentinite and fluid pathways in a subduction zone. Geology 39, 939–942. https://doi.org/10.1130/G32173.1

Kenkmann, T., Dresen, G., 2002. Dislocation microstructure and phase distribution in a lower crustal shear zone – an example from the Ivrea-Zone, Italy. International Journal of Earth Sciences 91, 445–458. https://doi.org/10.1007/s00531-001-0236-9

Kilian, R., Heilbronner, R., Stünitz, H., 2011. Quartz grain size reduction in a granitoid rock and the transition from dislocation to diffusion creep. Journal of Structural Geology 33, 1265–1284. https://doi.org/10.1016/j.jsg.2011.05.004

Kronenberg, A.K., Segall, P., Wolf, G.H., 1990. Hydrolytic weakening and penetrative deformation within a natural shear zone. In: Duba, A.G., Durham, W.B., Handin, J.W., Wang, H.F. (Eds.), The Brittle-Ductile Transition in Rocks, Geophysical Monograph Series. American Geophysical Union, Washington, D. C., 21–36. https://doi.org/10.1029/GM056p0021

Kruse, R., Stünitz, H., 1999. Deformation mechanisms and phase distribution in mafic high-temperature mylonites from the Jotun Nappe, southern Norway. Tectonophysics 303, 223–249. https://doi.org/10.1016/S0040-1951(98)00255-8

Kruse, R., Stünitz, H., Kunze, K., 2001. Dynamic recrystallization processes in plagioclase porphyroclasts. Journal of Structural Geology 23, 1781–1802. https://doi.org/10.1016/S0191-8141(01)00030-X

Langdon, T.G., 2009. Seventy-five years of superplasticity: historic developments and new opportunities. Journal of Materials Science 44, 5998–6010. https://doi.org/10.1007/s10853-009-3780-5

Langdon, T.G., 2006. Grain boundary sliding revisited: Developments in sliding over four decades. Journal of Materials Science 41, 597–609. https://doi.org/10.1007/s10853-006-6476-0

Langdon, T.G., 1993. The role of grain boundaries in high temperature deformation. Materials Science and Engineering: A 166, 67–79. https://doi.org/10.1016/0921-5093(93)90311-2

Langdon, T.G., 1991. The physics of superplastic deformation. Materials Science and Engineering: A, Fifth International Symposium on Plasticity of Metals and Alloys 137, 1–11. https://doi.org/10.1016/0921-5093(91)90312-B

Lapworth, T., Wheeler, J., Prior, D.J., 2002. The deformation of plagioclase investigated using electron backscatter diffraction crystallographic preferred orientation data. Journal of Structural Geology 24, 387–399. https://doi.org/10.1016/S0191-8141(01)00057-8

Lopez-Sanchez, M.A., Llana-Fúnez, S., 2018. A cavitation-seal mechanism for ultramylonite formation in quartzofeldspathic rocks within the semi-brittle field (Vivero fault, NW Spain). Tectonophysics 745, 132–153. https://doi.org/10.1016/j.tecto.2018.07.026

Lusk, A.D.J., Platt, J.P., Platt, J.A., 2021. Natural and Experimental Constraints on a Flow Law for Dislocation-Dominated Creep in Wet Quartz. Journal of Geophysical Research: Solid Earth 126, e2020JB021302. https://doi.org/10.1029/2020JB021302

Magloughlin, J.F., 1992. Microstructural and chemical changes associated with cataclasis and frictional melting at shallow crustal levels: the cataclasite-pseudotachylyte connection. Tectonophysics 204, 243–260. https://doi.org/10.1016/0040-1951(92)90310-3

Mancktelow, N.S., Pennacchioni, G., 2005. The control of precursor brittle fracture and fluid–rock interaction on the development of single and paired ductile shear zones. Journal of Structural Geology 27, 645–661. https://doi.org/10.1016/j.jsg.2004.12.001

Mandal, N., Misra, S., Kumar Samanta, S., 2004. Role of weak flaws in nucleation of shear zones: an experimental and theoretical study. Journal of Structural Geology 26, 1391–1400. https://doi.org/10.1016/j.jsg.2004.01.001

Maruyama, G., Hiraga, T., 2017. Grain- to multiple-grain-scale deformation processes during diffusion creep of forsterite + diopside aggregate: 2. Grain boundary sliding-induced grain rotation and its role in crystallographic preferred orientation in rocks. Journal of Geophysical Research: Solid Earth 122, 5916–5934. https://doi.org/10.1002/2017JB014255

Menegon, L., Pennacchioni, G., Spiess, R., 2008. Dissolution-precipitation creep of K-feldspar in mid-crustal granite mylonites. Journal of Structural Geology 30, 565–579. https://doi.org/10.1016/j.jsg.2008.02.001

Misra, S., Mandal, N., Dhar, R., Chakraborty, C., 2009. Mechanisms of deformation localization at the tips of shear fractures: Findings from analogue experiments and field evidence. Journal of Geophysical Research: Solid Earth 114. https://doi.org/10.1029/2008JB005737

Mitra, G., 1978. Ductile deformation zones and mylonites; the mechanical processes involved in the deformation of crystalline basement rocks. American Journal of Science 278, 1057–1084. https://doi.org/10.2475/ajs.278.8.1057

Mondal, M.E.A., Goswami, J.N., Deomurari, M.P., Sharma, K.K., 2002. Ion microprobe 207Pb/206Pb ages of zircons from the Bundelkhand massif, northern India: implications for crustal evolution of the Bundelkhand–Aravalli protocontinent. Precambrian Research 117, 85–100. https://doi.org/10.1016/S0301-9268(02)00078-5

Nadan, B.J., Engelder, T., 2009. Microcracks in New England granitoids: A record of thermoelastic relaxation during exhumation of intracontinental crust. GSA Bulletin 121, 80–99. https://doi.org/10.1130/B26202.1

Nguyen, N.T.-C., Asghari-Rad, P., Sathiyamoorthi, P., Zargaran, A., Lee, C.S., Kim, H.S., 2020. Ultrahigh high-strain-rate superplasticity in a nanostructured high-entropy alloy. Nature Communications 11, 2736. https://doi.org/10.1038/s41467-020-16601-1

Okudaira, T., Jeřábek, P., Stünitz, H., Fusseis, F., 2015. High-temperature fracturing and subsequent grain-size-sensitive creep in lower crustal gabbros: Evidence for coseismic loading followed by creep during decaying stress in the lower crust? Journal of Geophysical Research: Solid Earth 120, 3119–3141. https://doi.org/10.1002/2014JB011708

Okudaira, T., Shigematsu, N., 2012. Estimates of stress and strain rate in mylonites based on the boundary between the fields of grain-size sensitive and insensitive creep. Journal of Geophysical Research: Solid Earth 117. https://doi.org/10.1029/2011JB008799

Okudaira, T., Shigematsu, N., Harigane, Y., Yoshida, K., 2017. Grain size reduction due to fracturing and subsequent grain-size-sensitive creep in a lower crustal shear zone in the presence of a CO2-bearing fluid. Journal of Structural Geology 95, 171–187. https://doi.org/10.1016/j.jsg.2016.11.001

Park, Y., Yoo, S.-H., Ree, J.-H., 2006. Weakening of deforming granitic rocks with layer development at middle crust. Journal of Structural Geology 28, 919–928. https://doi.org/10.1016/j.jsg.2006.02.005

Passchier, C.W., 1984. The generation of ductile and brittle shear bands in a low-angle mylonite zone. Journal of Structural Geology 6, 273–281. https://doi.org/10.1016/0191-8141(84)90051-8

Passchier, C.W., Trouw, R.A.J., 2005. Microtectonics, 2nd ed. Springer-Verlag, Berlin/Heidelberg.

Pati, J.K., 2020. Evolution of Bundelkhand Craton. Episodes 43, 69–87. https://doi.org/10.18814/epiiugs/2020/020004

Pati, J.K., Patel, S.C., Pruseth, K.L., Malviya, V.P., Arima, M., Raju, S., Pati, P., Prakash, K., 2007. Geology and geochemistry of giant quartz veins from the Bundelkhand Craton, central India and their implications. Journal of Earth System Science 116, 497–510. https://doi.org/10.1007/s12040-007-0046-y

Pearce, M.A., Wheeler, J., Prior, D.J., 2011. Relative strength of mafic and felsic rocks during amphibolite facies metamorphism and deformation. Journal of Structural Geology 33, 662–675. https://doi.org/10.1016/j.jsg.2011.01.002

Pennacchioni, G., Mancktelow, N.S., 2018. Small-scale ductile shear zones: Neither extending, nor thickening, nor narrowing. Earth-Science Reviews 184, 1–12. https://doi.org/10.1016/j.earscirev.2018.06.004

Phillips, E.R., Ransom, D.M., Vernon, R.H., 1972. Myrmekite and muscovite developed by retrograde metamorphism at Broken Hill, New South Wales. Mineralogical Magazine 38, 570–578. https://doi.org/10.1180/minmag.1972.038.297.05

Platt, J.P., 2015. Rheology of two-phase systems: A microphysical and observational approach. Journal of Structural Geology 77, 213–227. https://doi.org/10.1016/j.jsg.2015.05.003

Précigout, J., Ledoux, E., Arbaret, L., Spriet, C., 2022. Porosity induced by dislocation dynamics in quartz-rich shear bands of granitic rocks. Scientific Reports 12, 6141. https://doi.org/10.1038/s41598-022-10053-x

Pryer, L.L., Robin, P.-Y.F., 1995. Retrograde metamorphic reactions in deforming granites and the origin of flame perthite. Journal of Metamorphic Geology 13, 645–658. https://doi.org/10.1111/j.1525-1314.1995.tb00249.x

Putnis, A., 2021. Fluid–Mineral Interactions: Controlling Coupled Mechanisms of Reaction, Mass Transfer and Deformation. Journal of Petrology 62, egab092. https://doi.org/10.1093/petrology/egab092

Ramsay, J.G., 1980. Shear zone geometry: A review. Journal of Structural Geology, Shear Zones in Rocks 2, 83–99. https://doi.org/10.1016/0191-8141(80)90038-3

Rao, J.M., Rao, G.P., Widdowson, M., Kelley, S., 2005. Evolution of Proterozoic mafic dyke swarms of the Bundelkhand Granite Massif, central India. Current Science 502–506.

Ree, J.-H., 1994. Grain boundary sliding and development of grain boundary openings in experimentally deformed octachloropropane. Journal of Structural Geology 16, 403–418. https://doi.org/10.1016/0191-8141(94)90044-2

Ribeiro, B.V., Faleiros, F.M., Campanha, G.A.C., Lagoeiro, L., Weinberg, R.F., Hunter, N.J.R., 2019. Kinematics, nature of deformation and tectonic setting of the Taxaquara Shear Zone, a major transpressional zone of the Ribeira Belt (SE Brazil). Tectonophysics 751, 83–108. https://doi.org/10.1016/j.tecto.2018.12.025

Rybacki, E., Dresen, G., 2004. Deformation mechanism maps for feldspar rocks. Tectonophysics 382, 173–187. https://doi.org/10.1016/j.tecto.2004.01.006

Rybacki, E., Paterson, M.S., Wirth, R., Dresen, G., 2003. Rheology of calcite–quartz aggregates deformed to large strain in torsion. Journal of Geophysical Research: Solid Earth 108. https://doi.org/10.1029/2002JB001833

Sacerdoti, M., Labernadière, H., Gandais, M., 1980. Transmission electron microscope (TEM) study of geologically deformed potassic feldspars. Bulletin de Minéralogie 103, 148–155. https://doi.org/10.3406/bulmi.1980.7388

Sarkar, G., Banerjee, S., Maity, S., Srivastava, H.B., 2020. Fluid assisted rejuvenation of precursor brittle fractures as the habitats of ductile shear zones: An example from the ~2.6 Ga Bundelkhand Granitoid of north-central India. Journal of Structural Geology 141, 104198. https://doi.org/10.1016/j.jsg.2020.104198

Schmid, S.M., Boland, J.N., Paterson, M.S., 1977. Superplastic flow in finegrained limestone. Tectonophysics 43, 257–291. https://doi.org/10.1016/0040-1951(77)90120-2

Schmid, S.M., Casey, M., 1986. Complete fabric analysis of some commonly observed quartz c-axis patterns. In: Hobbs, B.E., Heard, H.C. (Eds.), Mineral and Rock Deformation: Laboratory Studies. Geophysical Monograph Series. 36, 263–286. https://doi.org/10.1029/GM036p0263

Schulmann, K., Mlčoch, B., Melka, R., 1996. High-temperature microstructures and rheology of deformed granite, Erzgebirge, Bohemian Massif. Journal of Structural Geology 18, 719–733. https://doi.org/10.1016/S0191-8141(96)80007-1

Segall, P., Simpson, C., 1986. Nucleation of ductile shear zones on dilatant fractures. Geology 14, 56–59. https://doi.org/10.1130/0091-7613(1986)14<56:NODSZO>2.0.CO;2

Sensarma, S., Matin, A., Paul, D., Patra, A., Madhesiya, A.K., Sarkar, G., 2018. Reddening of ~2.5 Ga granitoid by high-temperature fluid linked to mafic dyke swarm in the Bundelkhand Craton, north central India. In: Rao, N.V. (Ed.), Geological Journal 53, 1338–1353. https://doi.org/10.1002/gj.2960

Sherby, O.D., Wadsworth, J., 1989. Superplasticity—Recent advances and future directions. Progress in Materials Science 33, 169–221. https://doi.org/10.1016/0079-6425(89)90004-2

Simpson, C., 1985. Deformation of granitic rocks across the brittle-ductile transition. Journal of Structural Geology 7, 503–511. https://doi.org/10.1016/0191-8141(85)90023-9

Simpson, C., Wintsch, R.P., 1989. Evidence for deformation-induced K-feldspar replacement by myrmekite. Journal of Metamorphic Geology 7, 261–275. https://doi.org/10.1111/j.1525-1314.1989.tb00588.x

Singh, S.P., Bhattacharya, A.R., 2017. N–S crustal shear system in the Bundelkhand massif: A unique crustal evolution signature in the northern Indian peninsula. Journal of Earth System Science 126, 121. https://doi.org/10.1007/s12040-017-0900-5

Singh, S.P., Bhattacharya, A.R., 2010. Signatures of Archaean E-W Crustal-Scale Shears in the Bundelkhand Massif, Central India: An Example of Vertical Ductile Shearing. 3, 9.

Singh, V.K., Slabunov, A., 2016. Two types of Archaean supracrustal belts in the Bundelkhand craton, India: Geology, geochemistry, age and implication for craton crustal evolution. Journal of the Geological Society of India 88, 539–548. https://doi.org/10.1007/s12594-016-0519-1

Skemer, P., Katayama, I., Jiang, Z., Karato, S., 2005. The misorientation index: Development of a new method for calculating the strength of lattice-preferred orientation. Tectonophysics 411, 157–167. https://doi.org/10.1016/j.tecto.2005.08.023

Soda, Y., Harigane, Y., Kajimoto, K., Okudaira, T., 2019. Crystallographic preferred orientations of plagioclase via grain boundary sliding in a lower-crustal anorthositic ultramylonite. International Journal of Earth Sciences 108, 2057–2069. https://doi.org/10.1007/s00531-019-01749-z

Song, Y., Zhao, S., Xu, C., 2021. Crystallographic orientation relationships between quartz and feldspar in myrmekite: a case study in monzodiorite from Meichuan pluton, China. Mineralogical Magazine 85, 406–415. https://doi.org/10.1180/mgm.2021.39

Spruzeniece, L., Piazolo, S., 2015. Strain localization in brittle–ductile shear zones: fluid-abundant vs. fluid-limited conditions (an example from Wyangala area, Australia). Solid Earth 6, 881–901. https://doi.org/10.5194/se-6-881-2015

Steffen, K., Selverstone, J., Brearley, A., 2001. Episodic weakening and strengthening during synmetamorphic deformation in a deep-crustal shear zone in the Alps. Geological Society, London, Special Publications 186, 141–156. https://doi.org/10.1144/GSL.SP.2001.186.01.09

Stipp, M., Stünitz, H., Heilbronner, R., Schmid, S.M., 2002. The eastern Tonale fault zone: a 'natural laboratory' for crystal plastic deformation of quartz over a temperature range from 250 to 700°C. Journal of Structural Geology 24, 1861–1884. https://doi.org/10.1016/S0191-8141(02)00035-4

Stünitz, H., Fitz Gerald, J.D., 1993. Deformation of granitoids at low metamorphic grade. II: Granular flow in albite-rich mylonites. Tectonophysics 221, 299–324. https://doi.org/10.1016/0040-1951(93)90164-F

Sullivan, W.A., Monz, M.E., 2016. Rheologic evolution of low-grade metasedimentary rocks and granite across a large strike-slip fault zone: A case study of the Kellyland fault zone, Maine, USA. Journal of Structural Geology 86, 13–31. https://doi.org/10.1016/j.jsg.2016.02.008

Tremblay, A., Malo, M., 1991. Significance of brittle and plastic fabrics within the Massawippi Lake fault zone, southern Canadian Appalachians. Journal of Structural Geology 13, 1013–1023. https://doi.org/10.1016/0191-8141(91)90053-L

Tullis, J., 2002. Deformation of Granitic Rocks: Experimental Studies and Natural Examples. Reviews in Mineralogy and Geochemistry 51, 51–95. https://doi.org/10.2138/gsrmg.51.1.51

Tullis, J., 1990. Experimental studies of deformation mechanisms and microstructures in quartzo-feldspathic rocks. In: Barber, D.J., Meredith, P.G. (Eds.), Deformation Processes in Minerals, Ceramics and Rocks, The Mineralogical Society Series. Springer Netherlands, Dordrecht, 190–227. https://doi.org/10.1007/978-94-011-6827-4_9

Tullis, J., Yund, R., Farver, J., 1996. Deformation-enhanced fluid distribution in feldspar aggregates and implications for ductile shear zones. Geology 24, 63–66. https://doi.org/10.1130/0091-7613(1996)024<0063:DEFDIF>2.3.CO;2

Tullis, J., Yund, R.A., 1991. Diffusion creep in feldspar aggregates: experimental evidence. Journal of Structural Geology 13, 987–1000. https://doi.org/10.1016/0191-8141(91)90051-J

Viegas, L.G.F., Archanjo, C.J., Hollanda, M.H.B.M., Vauchez, A., 2014. Microfabrics and zircon U–Pb (SHRIMP) chronology of mylonites from the Patos shear zone (Borborema Province, NE Brazil). Precambrian Research 243, 1–17. https://doi.org/10.1016/j.precamres.2013.12.020

Vollmer, F.W., 1990. An application of eigenvalue methods to structural domain analysis. GSA Bulletin 102, 786–791. https://doi.org/10.1130/0016-7606(1990)102<0786:AAOEMT>2.3.CO;2

Wheeler, J., Prior, D., Jiang, Z., Spiess, R., Trimby, P., 2001. The petrological significance of misorientations between grains. Contributions to Mineralogy and Petrology 141, 109–124. https://doi.org/10.1007/s004100000225

White, S., 1977. Geological significance of recovery and recrystallization processes in quartz. Tectonophysics 39, 143–170. https://doi.org/10.1016/0040-1951(77)90093-2

Whitney, D.L., Evans, B.W., 2010. Abbreviations for names of rock-forming minerals. American Mineralogist 95, 185–187. https://doi.org/10.2138/am.2010.3371

Wilson, C.J.L., 1975. Preferred Orientation in Quartz Ribbon Mylonites. GSA Bulletin 86, 968–974. https://doi.org/10.1130/0016-7606(1975)86<968:POIQRM>2.0.CO;2

Wintsch, R.P., Yeh, M.-W., 2013. Oscillating brittle and viscous behavior through the earthquake cycle in the Red River Shear Zone: Monitoring flips between reaction and textural softening and hardening. Tectonophysics, Deformation, Pophyroblasts and Mountain Building: A Special Issue in Honor of the Career Contributions of T.H. Bell 587, 46–62. https://doi.org/10.1016/j.tecto.2012.09.019

Zhang, Y., Hobbs, B.E., Jessell, M.W., 1994. The effect of grain-boundary sliding on fabric development in polycrystalline aggregates. Journal of Structural Geology 16, 1315–1325. https://doi.org/10.1016/0191-8141(94)90072-8

Zhou, B., Liu, J., Chen, X., Hou, C., 2022. Fluid-enhanced grain-size reduction of K-feldspar from a natural middle crustal shear zone in northern Beijing, China. Tectonophysics 838, 229478. https://doi.org/10.1016/j.tecto.2022.229478

Zuza, A.V., Cao, W., Rodriguez-Arriaga, A., DesOrmeau, J.W., Odlum, M.L., 2022. Strain localization at brittle-ductile transition depths during Miocene magmatism and exhumation in the southern Basin and Range. Journal of Structural Geology 163, 104709. https://doi.org/10.1016/j.jsg.2022.104709